

---

# Variational Sequential Optimal Experimental Design using Reinforcement Learning

---

**Wanggang Shen**

Department of Mechanical Engineering  
University of Michigan  
Ann Arbor, MI 48109  
wgshen@umich.edu

**Jiayuan Dong**

Department of Mechanical Engineering  
University of Michigan  
Ann Arbor, MI 48109  
jiayuand@umich.edu

**Xun Huan**

Department of Mechanical Engineering  
University of Michigan  
Ann Arbor, MI 48109  
xhuan@umich.edu

## Abstract

We introduce variational sequential Optimal Experimental Design (vsOED), a new method for optimally designing a finite sequence of experiments under a Bayesian framework and with information-gain utilities. Specifically, we adopt a lower bound estimator for the expected utility through variational approximation to the Bayesian posteriors. The optimal design policy is solved numerically by simultaneously maximizing the variational lower bound and performing policy gradient updates. We demonstrate this general methodology for a range of OED problems targeting parameter inference, model discrimination, and goal-oriented prediction. These cases encompass explicit and implicit likelihoods, nuisance parameters, and physics-based partial differential equation models. Our vsOED results indicate substantially improved sample efficiency and reduced number of forward model simulations compared to previous sequential design algorithms.

## 1 Introduction

Mathematical modeling is pivotal for understanding and describing the underlying processes of natural phenomena. Developing and refining models require experiment data, for example, to quantify and reduce the uncertainty among competing models and their parameters. However, experiments are often expensive and limited in number. Bayesian optimal experimental design (OED) [9, 41, 45, 44] provides a framework for systematically identifying the best conditions to perform experiments.

The objective function of Bayesian OED is generally the expected information gain (EIG) on model parameters (equivalent, expected Kullback-Leibler divergence or mutual information [37]). When this optimization is repeated for every new experiment, a greedy sequential design strategy is formed [14, 8, 51, 15, 16, 31, 25, 33]. However, greedy design ignores future consequences induced by early design decisions, and this lack of “planning ahead” renders the greedy policy sub-optimal.

The optimal formulation for sequential design [42, 52] and its computations through the lens of reinforcement learning (RL) have recently garnered attention. The works of [27, 29] provided a sequential OED (sOED) formulation through a finite-horizon Markov decision process (MDP) and proposed an approximate dynamic programming solution algorithm but is computationally expensive. [50] further reduced the cost of sOED by learning an explicit parameterized policy network and

utilizing the policy gradient. Elsewhere, [19] introduced the Deep Adaptive Design (DAD) that efficiently amortizes the inference cost by learning a policy network that instantaneously returns the next design given previous designs and observations, thereby greatly accelerating the online deployment speed. A variant, the Implicit DAD (iDAD) [30], is further furnished with the ability to accommodate implicit likelihoods. Since both DAD and iDAD use the forward model (i.e. parameter-to-observable map) derivative, [5] proposed to learn the policy using RL without this requirement. However, both this RL algorithm and DAD employ a nested Monte Carlo (MC) EIG lower bound that scales with  $\mathcal{O}(n^2)$  forward model evaluations, which remains costly since *each* forward model run may entail a partial differential equation (PDE) solve in many engineering and science settings [55].

To alleviate these computational requirements, we propose a novel variational sequential optimal experimental design (**vsOED**) method. The key idea of vsOED is to estimate and maximize an  $\mathcal{O}(n)$  lower bound formed through variational approximation of the Bayesian posteriors without needing explicit likelihood and prior. Notably, in contrast to existing sequential design algorithms that primarily focus on the EIG of model parameters within a single model, vsOED offers a *unified framework* that accommodates multi-model scenarios with diverse design objectives, including EIG for model probability, parameters of interest, and predictive quantities of interest, even in the presence of nuisance parameters. Furthermore, RL techniques are utilized to enhance the performance and efficiency of vsOED. We implement vsOED on benchmark problems and illustrate significantly improved sampling efficiency under fixed budgets of forward model runs, and also demonstrate with a physics-based model with PDE-governed dynamics.

## 2 Background

We focus on OED for a finite total of  $N$  experiments indexed by  $k \in \{0, \dots, N-1\}$ , where each experiment can be conducted under design  $d_k \in \mathcal{D}_k \subseteq \mathbb{R}^{N_d}$  and produces an observation  $y_k \in \mathbb{R}^{N_y}$ . The information sequence of all past experiments' designs and observations is denoted by  $I_k = [d_0, y_0, \dots, d_{k-1}, y_{k-1}]$  (with  $I_0 = \emptyset$ ). We further consider a discrete set of  $M$  candidate models indexed by  $m \in \{1, \dots, M\}$  for describing the experimental process. Each model contains unknown parameters of interest (PoIs)  $\theta_m \in \mathbb{R}^{N_{\theta_m}}$  we wish to learn from the experiments, nuisance parameters  $\eta_m \in \mathbb{R}^{N_{\eta_m}}$  that are uncertain but not targeted for learning, and associated predictive quantities of interest (QoIs)  $z_m \in \mathbb{R}^{N_{z_m}}$  that only depend on this model's parameters. For simplicity, we present these variables to be continuous and their dimensions remain constant across experiments; however this is not a requirement. The relationships of these entities may be summarized via an observation model

$$y_k = G_k(\theta_m, \eta_m, d_k; m, I_k) + \epsilon_k \quad (1)$$

where  $G_k$  is the observation forward mapping and  $\epsilon_k$  is the observation noise, and a predictive model

$$z_m = H(\theta_m, \eta_m; m) \quad (2)$$

where  $H$  is the predictive forward mapping. In many engineering and science systems, the forward mappings  $G_k$  and  $H$  involve the most expensive computations (e.g., solving systems of PDEs). Hence, the number of forward solves is often used as the unit for computational cost assessments.

Adopting a Bayesian approach, after the  $k$ th experiment is carried out, the joint probability density function (PDF) on  $m, \theta_m, \eta_m$  can be updated following Bayes' rule:

$$\begin{aligned} p(m, \theta_m, \eta_m | d_k, y_k, I_k) &= \frac{p(y_k | m, \theta_m, \eta_m, d_k, I_k) p(m, \theta_m, \eta_m | I_k)}{p(y_k | d_k, I_k)} \\ &= P(m | I_{k+1}) p(\theta_m, \eta_m | m, I_{k+1}), \end{aligned} \quad (3)$$

where  $p(m, \theta_m, \eta_m | I_k)$  is the prior,  $p(y_k | m, \theta_m, \eta_m, d_k, I_k)$  is the likelihood,  $p(y_k | d_k, I_k)$  is the marginal likelihood; and the joint posterior  $p(m, \theta_m, \eta_m | d_k, y_k, I_k)$  (and similarly for the prior) can be factored into product of  $P(m | I_{k+1})$  the posterior probability mass function (PMF) of model and  $p(\theta_m, \eta_m | m, I_{k+1})$  the posterior PDF of parameters conditioned on model  $m$ . In the remainder of this paper, we adopt the convention where when  $m$  is not explicitly mentioned, conditioning on  $m$  is implied through other variables' subscripts, e.g.,  $p(\theta_m, \eta_m | I_k) = p(\theta_m, \eta_m | m, I_k)$ . Upon propagating the parameter posterior through  $H$ , the posterior-predictive PDF for  $z_m$  becomes

$$p(z_m | I_{k+1}) = \int_{\Theta, \mathcal{H}} p(\theta_m, \eta_m | I_{k+1}) p(z_m | \theta_m, \eta_m) d\theta_m d\eta_m. \quad (4)$$

If  $H$  is a deterministic model, then  $p(z_m|\theta_m, \eta_m)$  collapses to a Dirac delta function.

The posterior after the  $k$ th experiment  $p(m, \theta_m, \eta_m|d_k, y_k, I_k) = p(m, \theta_m, \eta_m|I_{k+1})$  serves as the prior for the  $(k + 1)$ th experiment and is again applied to Eqn. (3). Hence, the Bayesian framework can be naturally and recursively used for sequential experiments, and it has long been demonstrated as an extended logic for expressing and updating uncertainty as new evidence becomes available [11].

## 2.1 Sequential optimal experimental design (sOED)

We present a RL-based formulation for sequential OED (sOED) following [50] and relevant earlier works of [27, 29]. Like any RL problem setup, this involves defining the core components of a Markov decision process (MDP).

**State.**  $x_k = [x_{k,b}, x_{k,p}] \in \mathcal{X}_k$  is the state of the system and environment prior to the  $k$ th experiment. The belief state  $x_{k,b}$  fully captures the state of uncertainty in  $m, \theta_m, \eta_m$ , and  $z_m$ , and the physical state  $x_{k,p}$  tracks any non-uncertain design-relevant quantities. The belief state conceptualizes as the posterior following a Bayesian paradigm for updating the rational belief about an outcome's plausibility [11, 17]. In practice, this amounts to numerically representing the posteriors in Eqn. (3) and (4) or their sufficient statistics. In this work, we adopt the trivial sufficient statistics of the posterior,  $I_k$ , which also captures the physical state since it records the history of all past experiments; hence,  $x_k = I_k$ . The main drawback is that  $\dim(I_k)$  grows with  $k$ , however it is always capped due to finite  $N$ .

**Design (action) and policy.**  $\pi = \{\mu_k : \mathcal{X}_k \mapsto \mathcal{D}_k\}_{k=0}^{N-1}$  is the deterministic policy mapping from state space to design (action) space. The design for the  $k$ th experiment is thus  $d_k = \mu_k(I_k)$ .

**State transition.**  $x_{k+1} = \mathcal{F}_k(x_k, d_k, y_k)$  describes the transition from state  $x_k$  to state  $x_{k+1}$  after conducting the  $k$ th experiment under design  $d_k$  and observing  $y_k$ . Since we represent the state using  $I_k$ , the transition is simply a concatenation  $I_{k+1} = [I_k, d_k, y_k]$ .

**Utility (reward).**  $g_k(I_k, d_k, y_k) \in \mathbb{R}$  denotes the immediate reward from the  $k$ th experiment, and  $g_N(I_N) \in \mathbb{R}$  is the terminal reward that can be only computed after all experiments are completed. Examples of information gain (IG)-based rewards will be provided in Sec. 2.2 and Sec. 2.3.

**Problem statement.** The sOED problem seeks the policy that maximizes the expected utility  $U$ :

$$\begin{aligned} \pi^* = \arg \max_{\pi = \{\mu_0, \dots, \mu_{N-1}\}} & \left\{ U(\pi) = \mathbb{E}_{I_N|\pi, I_0} \left[ \sum_{k=0}^{N-1} g_k(I_k, d_k, y_k) + g_N(I_N) \right] \right\} \\ \text{s.t.} & \quad d_k = \mu_k(I_k) \in \mathcal{D}_k, \\ & \quad I_{k+1} = [I_k, d_k, y_k], \quad \text{for } k = 0, \dots, N-1, \end{aligned} \quad (5)$$

This sOED framework has been shown to generalize the batch and sequential greedy designs [50].

## 2.2 Experimental design utilities

Following [37, 23], we propose two IG-based reward formulations.

1) *Terminal-information-gain (TIG)* targets the overall IG (Kullback-Leibler [KL] divergence) from all  $N$  experiments via the terminal reward:

$$\begin{aligned} g_k(I_k, d_k, y_k) &= 0, \quad k = 0, \dots, N-1 \\ g_N(I_N) &= \alpha_M D_{\text{KL}}(P(m|I_N) || P(m)) \\ &\quad + \mathbb{E}_{m|I_N} [\alpha_\Theta D_{\text{KL}}(p(\theta_m|I_N) || p(\theta_m)) + \alpha_Z D_{\text{KL}}(p(z_m|I_N) || p(z_m))], \end{aligned} \quad (7)$$

where  $\alpha_M \in [0, 1]$  (for model),  $\alpha_\Theta \in [0, 1]$  (for PoIs) and  $\alpha_Z \in [0, 1]$  (for QoIs) are the weights/switches of IG from the different variables. For example, setting  $\alpha_M = 1$  and  $\alpha_\Theta = \alpha_Z = 0$  reduces to only IG for model probability (OED for model discrimination);  $\alpha_\Theta = 1$  and  $\alpha_M = \alpha_Z = 0$  reduces to IG on PoIs (OED for inference);  $\alpha_Z = 1$  and  $\alpha_\Theta = \alpha_M = 0$  reduces to IG on QoIs (OED for goal-oriented prediction). In the special case when  $\alpha_M = \alpha_\Theta = 1$  and  $\alpha_Z = 0$ , or  $\alpha_M = \alpha_Z = 1$  and  $\alpha_\Theta = 0$ , the terminal reward is equivalent to  $D_{\text{KL}}(p(m, \theta_m|I_N) || p(m, \theta_m))$  and  $D_{\text{KL}}(p(m, z_m|I_N) || p(m, z_m))$ , respectively (Appendix A.1). When nuisance parameter  $\eta_m$  is absent, one should not set both  $\alpha_\Theta$  and  $\alpha_Z$  to 1, since the IG on  $z_m$  is fully absorbed into the IG on  $\theta_m$  (Appendix A.2).

2) *Incremental-information-gain (IIG)* adopts incremental IG for the immediate rewards:

$$g_k(I_k, d_k, y_k) = \alpha_M D_{\text{KL}}(P(m|I_{k+1}) || P(m|I_k)) + \mathbb{E}_{m|I_{k+1}} [\alpha_{\Theta} D_{\text{KL}}(p(\theta_m|I_{k+1}) || p(\theta_m|I_k)) + \alpha_Z D_{\text{KL}}(p(z_m|I_{k+1}) || p(z_m|I_k))], \quad k = 0, \dots, N-1 \quad (8)$$

$$g_N(I_N) = 0. \quad (9)$$

We denote  $U_T(\pi)$  to be the resulting sOED expected utility from Eqn. (5) when adopting the TIG rewards (Eqn. (6) and (7)), and  $U_I(\pi)$  when adopting the IIG rewards (Eqn. (8) and (9)).

**Theorem 1** (Terminal-incremental equivalence).  $U_T(\pi) = U_I(\pi)$  for any policy  $\pi$ .

A proof is provided in Appendix A.3. Hence, both formulations induce the same sOED problem.

### 2.3 One-point estimate for rewards

Direct evaluation of the expected utility requires repeated KL divergence (integral) estimates. Naïve estimates using grid discretization or MC integration would be highly expensive. Similar to [19], we propose one-point estimates that are much less costly. The 1) *one-point-TIG* formulation involves

$$\dot{g}_N(I_N) = \alpha_M \ln \frac{P(\dot{m}|I_N)}{P(\dot{m})} + \alpha_{\Theta} \ln \frac{p(\dot{\theta}_m|I_N)}{p(\dot{\theta}_m)} + \alpha_Z \ln \frac{p(\dot{z}_m|I_N)}{p(\dot{z}_m)} \quad (10)$$

with  $\dot{g}_k(I_k, d_k, y_k) = 0$  for  $k = 0, \dots, N-1$ ; and the 2) *one-point-IIG* involves

$$\dot{g}_k(I_k, d_k, y_k) = \alpha_M \ln \frac{P(\dot{m}|I_{k+1})}{P(\dot{m}|I_k)} + \alpha_{\Theta} \ln \frac{p(\dot{\theta}_m|I_{k+1})}{p(\dot{\theta}_m|I_k)} + \alpha_Z \ln \frac{p(\dot{z}_m|I_{k+1})}{p(\dot{z}_m|I_k)} \quad (11)$$

for  $k = 0, \dots, N-1$  and with  $\dot{g}_N(I_N) = 0$ . In the above,  $\dot{m}$ ,  $\dot{\theta}_m$ , and  $\dot{z}_m$  are the “true” sample values that generated the sequence  $I_N$  appearing in the conditionals. The corresponding *one-point estimate* expected utility is:

$$\dot{U}(\pi) = \mathbb{E}_{\dot{m}, \dot{\theta}_m, \dot{\eta}_m, \dot{z}_m} \mathbb{E}_{I_N | \pi, I_0, \dot{m}, \dot{\theta}_m, \dot{\eta}_m} \left[ \sum_{k=0}^{N-1} \dot{g}_k(I_k, d_k, y_k) + \dot{g}_N(I_N) \right]. \quad (12)$$

We denote  $\dot{U}_T(\pi)$  to be the resulting expected utility from Eqn. (12) when adopting the one-point-TIG rewards (Eqn. (10)), and  $\dot{U}_I(\pi)$  when adopting the one-point-IIG rewards (Eqn. (11)).

**Theorem 2** (One-point estimate equivalence).  $U_T(\pi) = \dot{U}_T(\pi) = \dot{U}_I(\pi) = U_I(\pi)$  for any policy  $\pi$ .

A proof is provided in Appendix A.4. Hence, both the original sOED and one-point estimate formulations, using either TIG or IIG, induce the same sOED problem. We note that for  $\dot{U}_I(\pi)$ , all the intermediate posteriors cancel out and only the prior  $p(\cdot)$  (i.e.  $p(\cdot|I_0)$ ) and the final posterior  $p(\cdot|I_N)$  survive. However, working with intermediate posteriors in the incremental rewards can lead to denser rewards that improves numerical performance [5]. For any expected utility form, the prior term  $p(\cdot)$  may be omitted since it would only result in an objective shift and not affect the arg-max (Appendix A.5). For cases when the prior is difficult to compute (e.g., prior-predictive  $p(z_m) = \int_{\Theta, \mathcal{H}} p(\theta_m, \eta_m) p(z_m|\theta_m, \eta_m) d\theta_m d\eta_m$  that needs to marginalize out  $\theta_m$  and  $\eta_m$ ), we will drop the prior term and use the shifted expected utility for policy optimization.

## 3 Variational sequential optimal experimental design (vsOED)

The one-point estimates proposed in Sec. 2.3 still require posterior density evaluations. Inspired by [20], we replace the true posteriors  $p(\cdot|I_k)$  with variational posterior approximations  $q(\cdot|I_k; \phi_{(\cdot)})$ , forming a lower bound estimator to the expected utility. The 1) *variational-one-point-TIG* becomes

$$\dot{g}_N(I_N; \phi) = \alpha_M \ln \frac{q(\dot{m}|I_N; \phi_M)}{P(\dot{m})} + \alpha_{\Theta} \ln \frac{q(\dot{\theta}_m|I_N; \phi_{\Theta_m})}{p(\dot{\theta}_m)} + \alpha_Z \ln \frac{q(\dot{z}_m|I_N; \phi_{Z_m})}{p(\dot{z}_m)} \quad (13)$$

with  $\dot{g}_k(I_k, d_k, y_k; \phi) = 0$  for  $k = 0, \dots, N - 1$ ; and the 2) *variational-one-point-IIG* becomes

$$\dot{g}_k(I_k, d_k, y_k; \phi) = \alpha_M \ln \frac{q(\dot{m}|I_{k+1}; \phi_M)}{q(\dot{m}|I_k; \phi_M)} + \alpha_\Theta \ln \frac{q(\dot{\theta}_m|I_{k+1}; \phi_{\Theta_m})}{q(\dot{\theta}_m|I_k; \phi_{\Theta_m})} + \alpha_Z \ln \frac{q(\dot{z}_m|I_{k+1}; \phi_{Z_m})}{q(\dot{z}_m|I_k; \phi_{Z_m})} \quad (14)$$

for  $k = 0, \dots, N - 1$  and with  $\dot{g}_N(I_N; \phi) = 0$ , and the understanding that  $q(\cdot|I_0; \phi_{(\cdot)})$  is  $p(\cdot|I_0)$ . The corresponding *variational one-point estimate* expected utility is:

$$\dot{U}(\pi; \phi) = \mathbb{E}_{\dot{m}, \dot{\theta}_m, \dot{\eta}_m, \dot{z}_m} \mathbb{E}_{I_N | \pi, I_0, \dot{m}, \dot{\theta}_m, \dot{\eta}_m} \left[ \sum_{k=0}^{N-1} \dot{g}_k(I_k, d_k, y_k; \phi) + \dot{g}_N(I_N; \phi) \right]. \quad (15)$$

Following similar ideas in non-sequential OED [20, 4], we show this to be a lower bound.

**Theorem 3** (Variational lower bound).  $\dot{U}(\pi; \phi) \leq \dot{U}(\pi) = U(\pi)$  for any policy  $\pi$  and variational posterior parameter  $\phi$ . The bound is tight if and only if  $q(\cdot|I_N; \phi_{(\cdot)}) = p(\cdot|I_N)$  (except the trivial case when  $\alpha_M = \alpha_\Theta = \alpha_Z = 0$ ).

A proof is provided in Appendix A.6. The **variational sOED (vsOED)** problem thus entails finding the optimal policy to maximize the lower bound, i.e.  $\pi^*, \phi^* = \arg \max_{\pi, \phi} \dot{U}(\pi; \phi)$ .

We note that the tightness of the bound does not depend on the quality of the intermediate variational posteriors (i.e.  $q(\cdot|I_k; \phi_{(\cdot)})$  for  $k = 1, \dots, N - 1$ ) due to their cancellations, and low-quality intermediate posterior approximation may be used (Appendix A.7). For example, when all intermediate posteriors are approximated by the prior, then the *one-point-IIG* collapses to the *one-point-TIG*. However, as we show in the results, good intermediate posterior approximations can lead to better numerical performance. Non-IG-based reward contributions (that do not depend on the posteriors) can also be incorporated into all previously introduced expected utility formulations without affecting any of the theorem results.

In our implementation, we employ a neural network (NN) to approximate the model posterior  $q(\dot{m}|I_k; \phi_M)$ , which takes  $d_k$ 's and  $y_k$ 's and uses a softmax output activation to produce each model's probability. For parameter posteriors  $q(\dot{\theta}_m|I_k; \phi_{\Theta_m})$  and  $q(\dot{z}_m|I_k; \phi_{Z_m})$ , we use independent Gaussian Mixture Models (GMMs) with NNs predicting the GMM weights, means, and standard deviations. Truncated Gaussian is used for parameter with compact support. We also test Normalizing Flows (NFs) for parameter posterior approximations. Further details are in Appendix B.1 and B.2.

## 4 Policy gradient and variational gradient for vsOED

We employ gradient-based methods to numerically solve for the optimal vsOED policy. To extract gradient, we explicitly parameterize policy  $\pi$  by  $w \in \mathbb{R}^{N_w}$  and denote the parameterized policy as  $\pi_w$ . Learning the policy (i.e. *actor*) explicitly offers significantly faster online usage [50, 19, 30, 5] compared to dynamic programming sOED [29] and myopic design that require solving new optimization problems at run time. Using parameterized policy, the vsOED problem becomes:

$$\begin{aligned} w^*, \phi^* &= \arg \max_{w, \phi} \dot{U}(w; \phi) \\ \text{s.t.} \quad & d_k = \mu_{k,w}(I_k) \in \mathcal{D}_k, \\ & I_{k+1} = [I_k, d_k, y_k], \quad \text{for } k = 0, \dots, N - 1. \end{aligned} \quad (16)$$

The gradient of the expected utility with respect to  $\phi$  can be trivially shown (Leibniz rule) to be:

$$\nabla_\phi \dot{U}(w; \phi) = \mathbb{E}_{\dot{m}, \dot{\theta}_m, \dot{\eta}_m, \dot{z}_m} \mathbb{E}_{I_N | \pi, I_0, \dot{m}, \dot{\theta}_m, \dot{\eta}_m} \left[ \sum_{k=0}^{N-1} \nabla_\phi \dot{g}_k(I_k, d_k, y_k; \phi) + \nabla_\phi \dot{g}_N(I_N; \phi) \right]. \quad (17)$$

The policy gradient can be derived near-identically following the proof in Appendix B of [50] except that the expressions for vsOED involve an additional outer expectation over  $\dot{m}, \dot{\theta}_m, \dot{\eta}_m, \dot{z}_m$ ; therefore the derivation is not repeated in this paper. The vsOED policy gradient is:

$$\nabla_w \dot{U}(w; \phi) = \mathbb{E}_{\dot{m}, \dot{\theta}_m, \dot{\eta}_m, \dot{z}_m} \sum_{k=0}^{N-1} \mathbb{E}_{I_k | \pi, I_0, \dot{m}, \dot{\theta}_m, \dot{\eta}_m} \left[ \nabla_w \mu_{k,w}(I_k) \nabla_{d_k} Q_k^{\pi_w}(I_k, d_k) \Big|_{d_k = \mu_{k,w}(I_k)} \right], \quad (18)$$

where  $Q_k^{\pi_w}$  is the *actor-value function* (i.e. *critic*) that quantifies the expected cumulative remaining reward for conducting  $k$ th experiment at design  $d_k$  and state  $I_k$  and thereafter following policy  $\pi_w$ .

In our implementation, we use NNs to parameterize both the actor and critic (architecture in Appendix B.3), with the critic parameters being  $\nu \in \mathbb{R}^{N\nu}$ . Details about the overall numerical algorithm can be found in the Appendix, including MC estimate of the variational gradient (Appendix B.4.1) and policy gradient (Appendix B.4.3), formulation and training of critic networks under TIG and IIG (Appendix B.4.2), exploration strategy (Appendix B.4.4), and hyperparameter tuning (Appendix B.4.5). The overall pseudocode is summarized in Algorithm 1.

---

**Algorithm 1:** The vsOED algorithm.

---

- 1: Initialize variational parameters  $\phi$ , actor (policy) parameters  $w$ , critic parameters  $\nu$ ;
  - 2: **for**  $l = 1, \dots, n_{\text{update}}$  **do**
  - 3:   Simulate  $n_{\text{episode}}$  episodes: sample  $m, \theta_m, \eta_m$  and  $z_m$  from the prior, and then for  $k = 0, \dots, N - 1$  sample  $d_k = \mu_{k,w}(I_k) + \epsilon_{\text{explore}}$  and  $y_k \sim p(y_k | m, \theta_m, \eta_m, d_k, I_k)$ ;
  - 4:   Update newly generated information sequences  $\left\{ I_N^{(i)} \right\}_{i=1}^{n_{\text{episode}}}$  into replay buffer;
  - 5:   Sample  $n_{\text{batch}}$  episodes from the replay buffer, update  $\phi$  and  $\left\{ \dot{g}_k^{(i)} \right\}_{i=1}^{n_{\text{batch}}}$  using sampled batch;
  - 6:   Estimate gradients and update  $\nu$  and  $w$  via gradient ascent using sampled batch;
  - 7: **end for**
  - 8: Return optimized policy network  $\pi_w$ ;
- 

## 5 Related work

Classical sequential Bayesian OED primarily uses greedy (myopic) design that maximizes the next-experiment’s expected utility only [14, 8, 51, 15, 16, 31, 25, 33], and therefore not optimal for the full design horizon. Efforts using an optimal sequential formulation accounting for future effects have been sparse [42, 52], and only recently benefited from advanced computational methods through RL-themed techniques [27, 29, 50, 19, 30, 5]. In both cases, IG-based utilities require estimating either the likelihood-evidence ratio using nested MC [46, 28] and Prior Contrastive Estimation (PCE) or other lower bounds [19, 21], or posterior-prior ratio involving posterior estimation from density discretization [29, 50], transport maps [29, 27], sequential MC [40], Laplace approximation [39], approximate Bayesian computation [38], variational lower bounds [20, 21], and direct density ratio estimation that is suitable for implicit likelihoods [34, 33].

While most of these efforts focused on OED for parameter inference, goal-oriented utilities targeting predictive QoIs have also been introduced for linear models [3] and made scalable to high dimensions leveraging low-rank methods [54]. Nuisance parameters in OED have been approached by additional MC marginalization [18]. More recently, [35] proposed various lower bound estimators that can handle nuisance parameter and model discrimination settings as well. These advanced utility formulations, however, are developed only for non-sequential OED.

## 6 Results and discussions

We validate and compare the performance of **vsOED** on a number of numerical experiments against baselines involving various *real-time* and *adaptive* algorithms (details in Appendix B.5). For **vsOED**, we employ GMMs and NFs for posterior approximation, and TIG and IIG reward formulations. We use the naming convention where, for example, **vsOED-G-I** stands for GMM with IIG, and **vsOED-N-T** for NF with TIG. Baseline methods include **Random** design, **DAD** [19], **iDAD** [30], and **RL** that employed advanced RL techniques [5]. **RL** can also be combined with both TIG and IIG, denoted by **RL-T** and **RL-I** respectively. **DAD** and **iDAD** require the derivative of the forward model, **vsOED** and **iDAD** can accommodate implicit likelihoods, and only **vsOED** can handle multi-model scenarios and model discrimination OED.

In order to maintain a consistent comparison platform, we will always use PCE [19, 5, 21] (Appendix C.3) to estimate the expected utility of different trained policies when possible. However, PCE cannot be used with nuisance parameters or predictive QoIs (i.e.  $\alpha_Z > 0$ ), in those cases

other measures are reported. In addition to the cases below, we also include a Constant Elasticity of Substitution example in Appendix C.5, but not presented in the main paper.

### 6.1 Source location finding

We adapt the source location finding problem from [19]. Our setup involves candidate models with  $m \in \{1, 2, 3\}$  sources randomly located in a 2D domain, each emitting a signal that decays inversely with the square of distance. The experimental observation is noise-corrupted signals, and the design is for finding the optimal sequence of observation locations to maximize the expected utility. A comprehensive presentation of various testing scenarios, including model discrimination OED, can be found in Appendix C.4. Below we only highlight the case where  $m$  fixed at 2 and so  $\alpha_M = 0$ .

The first case is a pure PoI (i.e. source locations) inference OED where  $\alpha_\Theta = 1$  and  $\alpha_Z = 0$ ; this is identical to the setup in previous literature [19, 30, 5]. Figure 1a presents the expected cumulative utilities at various experiment stages, where all policies are optimized for a design horizon of  $N = 30$  experiments and then evaluated on the various intermediate experiment stages. We restrict vsOED training to a total budget of 10 million episode samples, while fully training RL, DAD and iDAD using their default publication settings (RL 8 trillion episodes, DAD 100 billion episodes, and iDAD 200 million episodes). In this plot, vsOED with IIG achieves noticeably better expected utilities compared to TIG, while TIG still reaches similar performance as other fully trained baselines as they all produce comparable expected utilities at  $N = 30$ . The lower values for vsOED with TIG in the earlier stages suggest that the policy sacrifices short-term rewards for a higher total expected utility.

Figure 1b presents the expected utility versus design horizon  $N$ , where at each  $N$  the data point reflects a new policy optimized specifically for that horizon. We apply an equal computational budget of 10 million episodes for all methods. In this comparison, vsOED outperforms other baselines across all  $N$ . IIG again achieves better performance than TIG, especially for  $N > 15$ . The shaded regions in both Fig. 1a and 1b illustrate the robustness of vsOED, RL, and DAD training against random seeds, while iDAD exhibits some instability for longer horizons. Lastly, Fig. 2 provides a validation example showing that GMM can effectively approximate the posterior even when highly non-Gaussian.

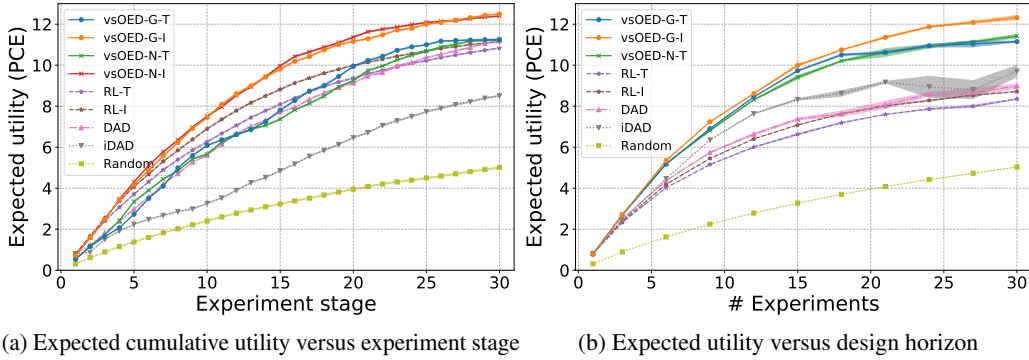


Figure 1: Expected utilities of various OED methods, all estimated using PCE with  $L = 10^6$ . (a) Mean and standard error (shaded) from 2000 evaluation episodes. (b) Mean and standard error (shaded) of 4 replicates with different random seeds, each replicate evaluated with 2000 episodes.

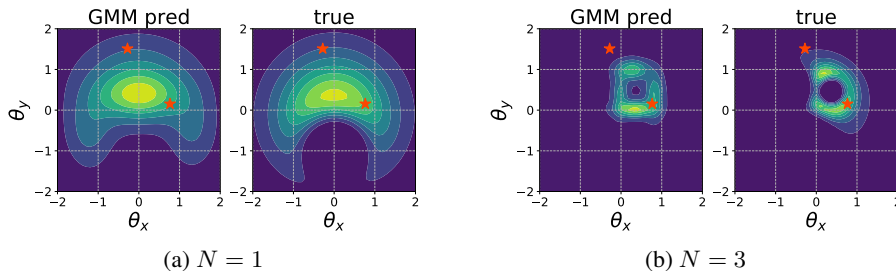


Figure 2: GMM posterior of PoIs versus their true posterior. Red stars are the true source locations.

The second case is a pure goal-oriented OED where  $\alpha_\Theta = 0$  and  $\alpha_Z = 1$ . The scenario is that the source is emitting a harmful contaminant posing a risk of populated area to the right of the domain. Our predictive QoI  $z$  is the contaminant flux integrated on the infinite vertical wall located at  $x = 6$ . Figure 3 contrasts the behavior of the PoI OED policy and the goal-oriented OED policy, where the former adjusts toward the estimated source locations while the latter forms a roughly vertical design pattern. This behavior can be explained from physical principles: since the flux is integrated over the  $y$ -coordinate, it is solely dependent on the  $x$ -position of the source (i.e.  $\theta_x$ ) (Appendix C.4). Spreading measurements along a vertical is more sensitive at detecting changes in  $\theta_x$  due to the isotropic nature of the source emission—this is supported by Fig. 4a showing the greater posterior shrinkage from a simple vertical sensor design over a simple horizontal sensor design. Figure 4b demonstrates that the GMM again successfully approximates the posterior-predictive of  $z$ .

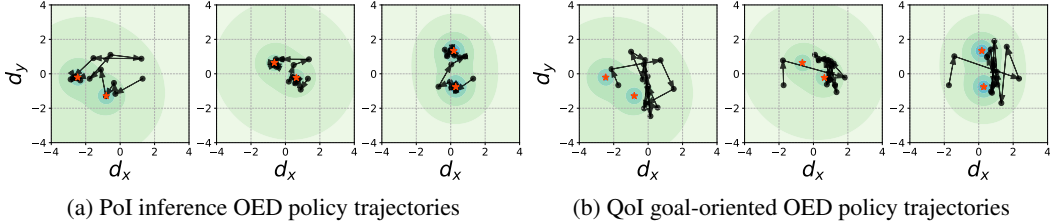


Figure 3: Policies for  $N = 15$ . The contour background illustrates the signal strength.

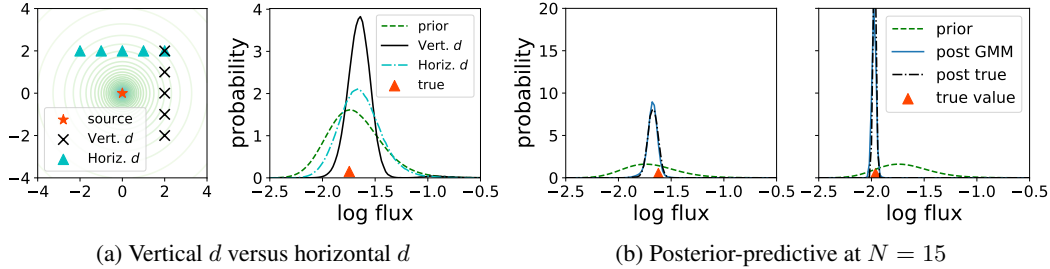


Figure 4: QoI posterior predictive comparisons for the goal-oriented OED.

## 6.2 SIR model

We demonstrate the ability of vsOED to handle implicit likelihood via the SIR example from [30]. SIR is a stochastic model [35, 10] describing the spread of infectious diseases in a population. Individuals in the population are divided into three categories: susceptible, infected, and recovered. Transitions among these categories are governed by the infection rate and recovery rate parameters. The design problem entails identifying time points for measuring the number of infected individuals so that the PoI can be best inferred. Solving the underlying stochastic differential equation is expensive, we thus limit the computational budget to 1 million forward model simulations for both vsOED and iDAD. Figure 5a illustrates the variational lower bound of the expected utility. vsOED and iDAD perform similarly, with vsOED slightly better in some cases. However, we note that the comparison is not entirely commensurable since the two methods use different variational lower bounds, and that iDAD additionally uses the forward model derivative. A potential benefit for vsOED is that it does not require forward model derivative, which can be valuable where model derivative is inaccessible. Figure 5b shows an example posterior generated from the GMM, which we see is consistent with the true data-generating values. Appendix C.6 contains additional details on the SIR example.

## 6.3 Convection-diffusion

The last example entails finding the optimal sensor movement locations within a chemical contaminant plume governed by the 2D convection-diffusion PDE. We consider three candidate models with  $m \in \{1, 2, 3\}$  randomly located chemical sources. The PoIs are the source locations, nuisance parameters are the convection speed and direction, and predictive QoI is the integrated flux along the right boundary. A sensor movement penalty is also present in the immediate rewards. To expedite the

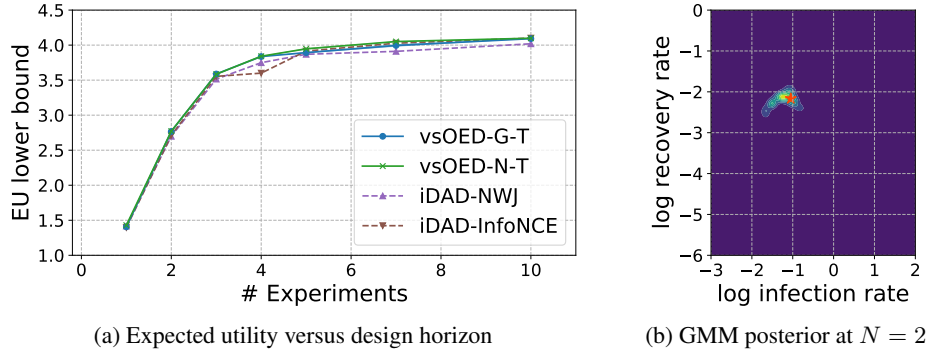


Figure 5: (a) vsOED plot is the mean and standard error (shaded) from 4 replicates with different random seeds, each replicate evaluated with  $3 \times 10^5$  episodes. Shaded regions are practically invisible, suggesting robustness. (b) An example posterior generated from the GMM.

training process, we pre-construct a NN surrogate model from the PDE and utilize it as the forward model. More details can be found in Appendix C.7. Figure 6 shows the policy and posterior for a pure model discrimination OED where  $\alpha_M = 1$  and  $\alpha_\Theta = \alpha_Z = 0$ . The policy behavior is more exploratory often extending to the boundaries of the domain, leading to a high IG (narrow posterior) on model probability as shown in Fig. 6b. Figure 7 presents the pure PoI inference OED ( $\alpha_\Theta = 1$  and  $\alpha_M = \alpha_Z = 0$ ) and pure QoI goal-oriented OED ( $\alpha_Z = 1$  and  $\alpha_M = \alpha_\Theta = 0$ ) policies. The inference OED policy appears to explore closer around the estimated sources while leveraging the background convection, and the goal-oriented policy exhibits a similar vertical design tendency as explained in the Sec. 6.1 example.

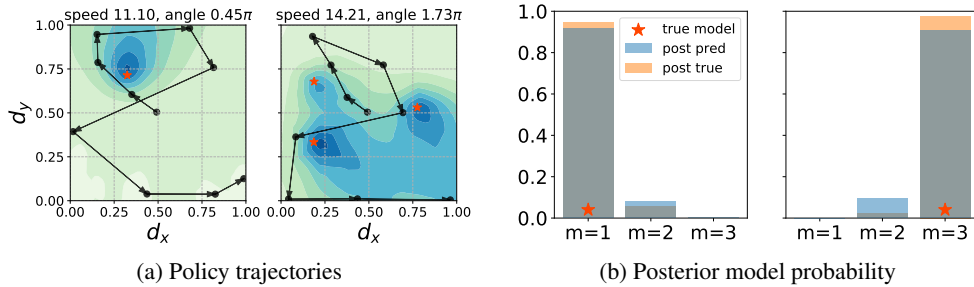


Figure 6: Convection-diffusion model discrimination OED results at  $N = 10$ .

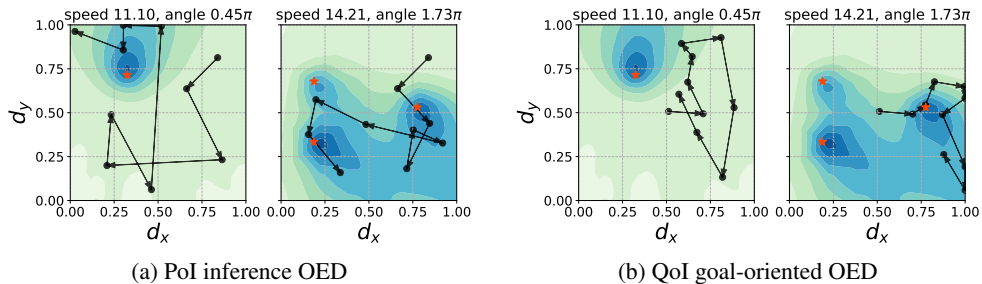


Figure 7: Convection-diffusion inference OED and goal-oriented OED policy comparisons at  $N = 10$ .

## 7 Conclusion

In this paper, we introduced vsOED, a sample-efficient method for Bayesian sequential OED that can handle implicit models and multi-model scenarios, and accommodate diverse OED objectives (parameter inference, model discrimination, goal-oriented prediction). Leveraging variational approximation and policy gradient, vsOED demonstrated superior performance in the explicit likelihood setting under fixed computational budget, while achieving similar performance as iDAD in the implicit likelihood setting without needing forward model derivatives. A limitation of vsOED is its sensitivity to inaccurate posterior representations, which can lead to suboptimal policies when the posteriors are challenging to approximate. Future work for developing accurate and adaptive posterior representations especially in high dimensions, as well as utilizing other variational bounds [30, 43], will be important. The current algorithm also does not consider discrete designs or stochastic policies, which when enabled, can reach a wider class of design problems. vsOED performance can also be further enhanced through advanced RL techniques [48, 47, 24, 22].

## Acknowledgments and Disclosure of Funding

This research is based upon work supported in part by the U.S. Department of Energy, Office of Science, Office of Advanced Scientific Computing Research, under Award Numbers DE-SC0021397 and DE-SC0021398. This paper was prepared as an account of work sponsored by an agency of the United States Government. Neither the United States Government nor any agency thereof, nor any of their employees, makes any warranty, express or implied, or assumes any legal liability or responsibility for the accuracy, completeness, or usefulness of any information, apparatus, product, or process disclosed, or represents that its use would not infringe privately owned rights. Reference herein to any specific commercial product, process, or service by trade name, trademark, manufacturer, or otherwise does not necessarily constitute or imply its endorsement, recommendation, or favoring by the United States Government or any agency thereof. The views and opinions of authors expressed herein do not necessarily state or reflect those of the United States Government or any agency thereof.

## References

- [1] L. J. Allen. A primer on stochastic epidemic models: Formulation, numerical simulation, and analysis. *Infectious Disease Modelling*, 2(2):128–142, 2017.
- [2] K. J. Arrow, H. B. Chenery, B. S. Minhas, and R. M. Solow. Capital-labor substitution and economic efficiency. *The review of Economics and Statistics*, pages 225–250, 1961.
- [3] A. Attia, A. Alexanderian, and A. K. Saibaba. Goal-oriented optimal design of experiments for large-scale Bayesian linear inverse problems. *Inverse Problems*, 34(9):095009, 2018.
- [4] D. Barber and F. Agakov. The IM algorithm: a variational approach to information maximization. *Advances in neural information processing systems*, 16(320):201, 2004.
- [5] T. Blau, E. V. Bonilla, I. Chades, and A. Dezfouli. Optimizing Sequential Experimental Design with Deep Reinforcement Learning. In *International Conference on Machine Learning*, pages 2107–2128. PMLR, 2022.
- [6] D. M. Borth. A total entropy criterion for the dual problem of model discrimination and parameter estimation. *Journal of the Royal Statistical Society: Series B (Methodological)*, 37(1):77–87, 1975.
- [7] J. Burkardt. The truncated normal distribution. *Department of Scientific Computing Website, Florida State University*, 1:35, 2014.
- [8] D. R. Cavagnaro, J. I. Myung, M. A. Pitt, and J. V. Kujala. Adaptive Design Optimization: A Mutual Information-Based Approach to Model Discrimination in Cognitive Science. *Neural Computation*, 22(4):887–905, 2010.
- [9] K. Chaloner and I. Verdinelli. Bayesian Experimental Design: A Review. *Statistical Science*, 10(3):273–304, 1995.
- [10] A. R. Cook, G. J. Gibson, and C. A. Gilligan. Optimal observation times in experimental epidemic processes. *Biometrics*, 64(3):860–868, 2008.
- [11] R. T. Cox. Probability, Frequency and Reasonable Expectation. *American Journal of Physics*, 14(1):1–13, 1946.
- [12] K. Csilléry, M. G. Blum, O. E. Gaggiotti, and O. François. Approximate bayesian computation (abc) in practice. *Trends in ecology & evolution*, 25(7):410–418, 2010.
- [13] L. Dinh, J. N. Sohl-Dickstein, and S. Bengio. Density estimation using Real NVP. *arXiv preprint arXiv:1605.08803*, 2016.
- [14] H. A. Dror and D. M. Steinberg. Sequential Experimental Designs for Generalized Linear Models. *Journal of the American Statistical Association*, 103(481):288–298, 2008.
- [15] C. C. Drovandi, J. M. McGree, and A. N. Pettitt. Sequential Monte Carlo for Bayesian sequentially designed experiments for discrete data. *Computational Statistics & Data Analysis*, 57(1):320–335, 2013.
- [16] C. C. Drovandi, J. M. McGree, and A. N. Pettitt. A Sequential Monte Carlo Algorithm to Incorporate Model Uncertainty in Bayesian Sequential Design. *Journal of Computational and Graphical Statistics*, 23(1):3–24, 2014.
- [17] J. A. Duersch and T. A. Catanach. Generalizing Information to the Evolution of Rational Belief. *Entropy*, 22(1):108, 2020.
- [18] C. Feng and Y. M. Marzouk. A layered multiple importance sampling scheme for focused optimal Bayesian experimental design. *arXiv preprint arXiv:1903.11187*, 2019.
- [19] A. Foster, D. R. Ivanova, I. Malik, and T. Rainforth. Deep adaptive design: Amortizing sequential Bayesian experimental design. In *International Conference on Machine Learning*, pages 3384–3395. PMLR, 2021.
- [20] A. Foster, M. Jankowiak, E. Bingham, P. Horsfall, Y. W. Teh, T. Rainforth, and N. Goodman. Variational Bayesian Optimal Experimental Design. In *33rd Conference on Neural Information Processing Systems (NeurIPS 2019)*, Vancouver, Canada, 2019.
- [21] A. Foster, M. Jankowiak, M. O’Meara, Y. W. Teh, and T. Rainforth. A unified stochastic gradient approach to designing Bayesian-optimal experiments. In *International Conference on Artificial Intelligence and Statistics*, pages 2959–2969. PMLR, 2020.

- [22] S. Fujimoto, H. Hoof, and D. Meger. Addressing function approximation error in actor-critic methods. In *International conference on machine learning*, pages 1587–1596. PMLR, 2018.
- [23] J. Ginebra. On the Measure of the Information in a Statistical Experiment. *Bayesian Analysis*, 2(1):167–212, 2007.
- [24] T. Haarnoja, A. Zhou, P. Abbeel, and S. Levine. Soft actor-critic: Off-policy maximum entropy deep reinforcement learning with a stochastic actor. In *International Conference on Machine Learning*, pages 1861–1870. PMLR, 2018.
- [25] M. Hainy, C. C. Drovandi, and J. M. McGree. Likelihood-free extensions for bayesian sequentially designed experiments. In J. Kunert, C. H. Müller, and A. C. Atkinson, editors, *mODa 11 - Advances in Model-Oriented Design and Analysis*, pages 153–161, Cham, 2016. Springer International Publishing.
- [26] H. Hasselt. Double q-learning. *Advances in neural information processing systems*, 23, 2010.
- [27] X. Huan. *Numerical Approaches for Sequential Bayesian Optimal Experimental Design*. PhD thesis, Massachusetts Institute of Technology, 2015.
- [28] X. Huan and Y. M. Marzouk. Simulation-based optimal Bayesian experimental design for nonlinear systems. *Journal of Computational Physics*, 232(1):288–317, 2013.
- [29] X. Huan and Y. M. Marzouk. Sequential Bayesian optimal experimental design via approximate dynamic programming. *arXiv preprint arXiv:1604.08320*, 2016.
- [30] D. R. Ivanova, A. Foster, S. Kleinegesse, M. U. Gutmann, and T. Rainforth. Implicit deep adaptive design: policy-based experimental design without likelihoods. *Advances in Neural Information Processing Systems*, 34:25785–25798, 2021.
- [31] W. Kim, M. A. Pitt, Z.-L. Lu, M. Steyvers, and J. I. Myung. A Hierarchical Adaptive Approach to Optimal Experimental Design. *Neural Computation*, 26:2565–2492, 2014.
- [32] D. P. Kingma and J. Ba. Adam: A method for stochastic optimization. *arXiv preprint arXiv:1412.6980*, 2014.
- [33] S. Kleinegesse, C. Drovandi, and M. U. Gutmann. Sequential Bayesian Experimental Design for Implicit Models via Mutual Information. *Bayesian Analysis*, 16(3):773–802, sep 2021.
- [34] S. Kleinegesse and M. U. Gutmann. Bayesian Experimental Design for Implicit Models by Mutual Information Neural Estimation. *arXiv preprint arXiv:2002.08129*, 2020.
- [35] S. Kleinegesse and M. U. Gutmann. Gradient-based Bayesian experimental design for implicit models using mutual information lower bounds. *arXiv preprint arXiv:2105.04379*, 2021.
- [36] T. P. Lillicrap, J. J. Hunt, A. Pritzel, N. Heess, T. Erez, Y. Tassa, D. Silver, and D. Wierstra. Continuous control with deep reinforcement learning. *arXiv preprint arXiv:1509.02971*, 2015.
- [37] D. V. Lindley. On a Measure of the Information Provided by an Experiment. *The Annals of Mathematical Statistics*, 27(4):986–1005, 1956.
- [38] J. Lintusaari, M. U. Gutmann, R. Dutta, S. Kaski, and J. Corander. Fundamentals and Recent Developments in Approximate Bayesian Computation. *Systematic Biology*, 66:e66 – e82, 2016.
- [39] Q. Long, M. Scavino, R. Tempone, and S. Wang. Fast estimation of expected information gains for Bayesian experimental designs based on Laplace approximations. *Computer Methods in Applied Mechanics and Engineering*, 259:24–39, 2013.
- [40] H. Moffat, M. Hainy, N. E. Papanikolaou, and C. Drovandi. Sequential experimental design for predator–prey functional response experiments. *Journal of The Royal Society Interface*, 17(166):20200156, 2020.
- [41] P. Müller. Simulation Based Optimal Design. *Handbook of Statistics*, 25:509–518, 2005.
- [42] P. Müller, D. A. Berry, A. P. Grieve, M. Smith, and M. Krams. Simulation-based sequential Bayesian design. *Journal of Statistical Planning and Inference*, 137(10):3140–3150, 2007.
- [43] B. Poole, S. Ozair, A. Van Den Oord, A. Alemi, and G. Tucker. On variational bounds of mutual information. In *International Conference on Machine Learning*, pages 5171–5180. PMLR, 2019.
- [44] T. Rainforth, A. Foster, D. R. Ivanova, and F. B. Smith. Modern Bayesian Experimental Design. *arXiv preprint arXiv:2302.14545*, 2023.

- [45] E. G. Ryan, C. C. Drovandi, J. M. McGree, and A. N. Pettitt. A Review of Modern Computational Algorithms for Bayesian Optimal Design. *International Statistical Review*, 84(1):128–154, 2016.
- [46] K. J. Ryan. Estimating Expected Information Gains for Experimental Designs With Application to the Random Fatigue-Limit Model. *Journal of Computational and Graphical Statistics*, 12(3):585–603, 2003.
- [47] J. Schulman, S. Levine, P. Abbeel, M. Jordan, and P. Moritz. Trust region policy optimization. In *International conference on machine learning*, pages 1889–1897, 2015.
- [48] J. Schulman, F. Wolski, P. Dhariwal, A. Radford, and O. Klimov. Proximal policy optimization algorithms. *arXiv preprint arXiv:1707.06347*, 2017.
- [49] D. W. Scott. *Multivariate density estimation: theory, practice, and visualization*. John Wiley & Sons, 2015.
- [50] W. Shen and X. Huan. Bayesian sequential optimal experimental design for nonlinear models using policy gradient reinforcement learning. *arXiv preprint arXiv:2110.15335*, 2021.
- [51] A. Solonen, H. Haario, and M. Laine. Simulation-Based Optimal Design Using a Response Variance Criterion. *Journal of Computational and Graphical Statistics*, 21(1):234–252, 2012.
- [52] U. Von Toussaint. Bayesian inference in physics. *Reviews of Modern Physics*, 83:943–999, 2011.
- [53] R. J. Williams. Simple statistical gradient-following algorithms for connectionist reinforcement learning. *Machine learning*, 8(3):229–256, 1992.
- [54] K. Wu, P. Chen, and O. Ghattas. An efficient method for goal-oriented linear Bayesian optimal experimental design: Application to optimal sensor placement. *arXiv preprint arXiv:2102.06627*, 2021.
- [55] K. Wu, P. Chen, and O. Ghattas. A Fast and Scalable Computational Framework for Large-Scale High-Dimensional Bayesian Optimal Experimental Design. *SIAM/ASA Journal on Uncertainty Quantification*, 11:235–261, 03 2023.

## A Proofs

### A.1 Information gain jointly with model probability

Akin to the total entropy described in [6], the information gain (IG) jointly on the model probability and model parameters of interest (PoIs) is:

$$\begin{aligned}
& D_{\text{KL}}(p(m, \theta_m | I_{k_2}) || p(m, \theta_m | I_{k_1})) \\
&= \sum_{m=1}^M \int_{\Theta} p(m, \theta_m | I_{k_2}) \ln \frac{p(m, \theta_m | I_{k_2})}{p(m, \theta_m | I_{k_1})} d\theta_m \\
&= \sum_{m=1}^M P(m | I_{k_2}) \int_{\Theta} p(\theta_m | I_{k_2}) \ln \frac{P(m | I_{k_2}) p(\theta_m | I_{k_2})}{P(m | I_{k_1}) p(\theta_m | I_{k_1})} d\theta_m \\
&= \sum_{m=1}^M P(m | I_{k_2}) \ln \frac{P(m | I_{k_2})}{P(m | I_{k_1})} + \sum_{m=1}^M P(m | I_{k_2}) \int_{\Theta} p(\theta_m | I_{k_2}) \ln \frac{p(\theta_m | I_{k_2})}{p(\theta_m | I_{k_1})} d\theta_m \\
&= D_{\text{KL}}(P(m | I_{k_2}) || P(m | I_{k_1})) + \mathbb{E}_{m | I_{k_2}} [D_{\text{KL}}(p(\theta_m | I_{k_2}) || p(\theta_m | I_{k_1}))],
\end{aligned}$$

where  $0 \leq k_1 \leq k_2 \leq N$ . Note that we use the convention where when  $m$  is not explicitly mentioned, conditioning on  $m$  is implied through other variables' subscripts, e.g.,  $p(\theta_m | I_k) = p(\theta_m | m, I_k)$ . When setting  $k_1 = 0$  and  $k_2 = N$ , we recover the terminal reward in Eqn. (7) under the special case of  $\alpha_M = \alpha_{\Theta} = 1$  and  $\alpha_Z = 0$ .

Similarly, the IG jointly on the model probability and predictive quantities of interest (QoIs) is:

$$\begin{aligned}
& D_{\text{KL}}(p(m, z_m | I_{k_2}) || p(m, z_m | I_{k_1})) \\
&= \sum_{m=1}^M \int_Z p(m, z_m | I_{k_2}) \ln \frac{p(m, z_m | I_{k_2})}{p(m, z_m | I_{k_1})} dz_m \\
&= \sum_{m=1}^M P(m | I_{k_2}) \int_Z p(z_m | I_{k_2}) \ln \frac{P(m | I_{k_2}) p(z_m | I_{k_2})}{P(m | I_{k_1}) p(z_m | I_{k_1})} dz_m \\
&= \sum_{m=1}^M P(m | I_{k_2}) \frac{P(m | I_{k_2})}{P(m | I_{k_1})} + \sum_{m=1}^M P(m | I_{k_2}) \int_Z p(z_m | I_{k_2}) \ln \frac{p(z_m | I_{k_2})}{p(z_m | I_{k_1})} dz_m \\
&= D_{\text{KL}}(P(m | I_{k_2}) || P(m | I_{k_1})) + \mathbb{E}_{m | I_{k_2}} [D_{\text{KL}}(p(z_m | I_{k_2}) || p(z_m | I_{k_1}))],
\end{aligned}$$

where  $0 \leq k_1 \leq k_2 \leq N$ . When setting  $k_1 = 0$  and  $k_2 = N$ , we recover the terminal reward in Eqn. (7) under the special case of  $\alpha_M = \alpha_Z = 1$  and  $\alpha_{\Theta} = 0$ .

### A.2 Information gain jointly on model parameters and predictive quantities

When the nuisance parameters  $\eta_m$  are absent, the IG jointly on the PoIs and QoIs given model  $m$  is:

$$\begin{aligned}
& D_{\text{KL}}(p(\theta_m, z_m | I_{k_2}) || p(\theta_m, z_m | I_{k_1})) \\
&= \int_{\Theta, Z} p(\theta_m, z_m | I_{k_2}) \ln \frac{p(\theta_m, z_m | I_{k_2})}{p(\theta_m, z_m | I_{k_1})} dz_m d\theta_m \\
&= \int_{\Theta, Z} p(\theta_m, z_m | I_{k_2}) \ln \frac{p(\theta_m | I_{k_2}) p(z_m | \theta_m, I_{k_2})}{p(\theta_m | I_{k_1}) p(z_m | \theta_m, I_{k_1})} dz_m d\theta_m \\
&= \int_{\Theta, Z} p(\theta_m, z_m | I_{k_2}) \ln \frac{p(\theta_m | I_{k_2}) p(z_m | \theta_m)}{p(\theta_m | I_{k_1}) p(z_m | \theta_m)} dz_m d\theta_m \\
&= \int_{\Theta, Z} p(\theta_m, z_m | I_{k_2}) \ln \frac{p(\theta_m | I_{k_2})}{p(\theta_m | I_{k_1})} dz_m d\theta_m \\
&= \int_{\Theta} p(\theta_m | I_{k_2}) \ln \frac{p(\theta_m | I_{k_2})}{p(\theta_m | I_{k_1})} d\theta_m \\
&= D_{\text{KL}}(p(\theta_m | I_{k_2}) || p(\theta_m | I_{k_1})),
\end{aligned}$$

where the third equality is due to  $z_m$  only dependent on  $\theta_m$  when  $\eta_m$  is absent (see Eqn. (2)). Hence, the IG on the QoIs is fully absorbed into the IG on the PoIs when nuisance parameters are absent.

### A.3 Proof of Theorem 1 (Terminal-incremental equivalence)

*Proof.* We first decompose  $U_T(\pi)$  into four additive parts:

$$U_T(\pi) = U_T(\pi; \text{non-IG}) + U_T(\pi; \alpha_M) + U_T(\pi; \alpha_\Theta) + U_T(\pi; \alpha_Z),$$

where  $U_T(\pi; \text{non-IG})$  captures any non-IG reward contributions, and the other three parts are (while explicitly writing out  $I_0$ )

$$\begin{aligned} U_T(\pi; \alpha_M) &= \alpha_M \mathbb{E}_{I_N|\pi, I_0} [D_{\text{KL}}(P(m|I_N) || P(m|I_0))] \\ U_T(\pi; \alpha_\Theta) &= \alpha_\Theta \mathbb{E}_{I_N|\pi, I_0} \mathbb{E}_{m|I_N} [D_{\text{KL}}(p(\theta_m|I_N) || p(\theta_m|I_0))] \\ U_T(\pi; \alpha_Z) &= \alpha_Z \mathbb{E}_{I_N|\pi, I_0} \mathbb{E}_{m|I_N} [D_{\text{KL}}(p(z_m|I_N) || p(z_m|I_0))]. \end{aligned}$$

Similarly,  $U_I(\pi)$  can also be decomposed into four additive parts:

$$U_I(\pi) = U_I(\pi; \text{non-IG}) + U_I(\pi; \alpha_M) + U_I(\pi; \alpha_\Theta) + U_I(\pi; \alpha_Z),$$

where  $U_I(\pi; \text{non-IG})$  captures any non-IG reward contributions, and the other three parts are (while explicitly writing out  $I_0$ )

$$\begin{aligned} U_I(\pi; \alpha_M) &= \alpha_M \mathbb{E}_{I_N|\pi, I_0} \left[ \sum_{k=0}^{N-1} D_{\text{KL}}(P(m|I_{k+1}) || P(m|I_k)) \right] \\ U_I(\pi; \alpha_\Theta) &= \alpha_\Theta \mathbb{E}_{I_N|\pi, I_0} \sum_{k=0}^{N-1} \mathbb{E}_{m|I_{k+1}} [D_{\text{KL}}(p(\theta_m|I_{k+1}) || p(\theta_m|I_k))] \\ U_I(\pi; \alpha_Z) &= \alpha_Z \mathbb{E}_{I_N|\pi, I_0} \sum_{k=0}^{N-1} \mathbb{E}_{m|I_{k+1}} [D_{\text{KL}}(p(z_m|I_{k+1}) || p(z_m|I_k))]. \end{aligned}$$

Since TIG and IIG formulations only entail the IG contributions, the non-IG reward contributions are therefore not affected by this choice and hence

$$U_T(\pi; \text{non-IG}) = U_I(\pi; \text{non-IG}).$$

For the part corresponding to IG on model probability:

$$\begin{aligned}
& U_I(\pi; \alpha_M) - U_T(\pi; \alpha_M) \\
&= \alpha_M \mathbb{E}_{I_N|\pi, I_0} \left[ \sum_{k=0}^{N-1} D_{\text{KL}}(P(m|I_{k+1}) || P(m|I_k)) - D_{\text{KL}}(P(m|I_N) || P(m|I_0)) \right] \\
&= \alpha_M \mathbb{E}_{I_N|\pi, I_0} \left[ \sum_{k=0}^{N-1} \sum_{m=1}^M P(m|I_{k+1}) \ln \frac{P(m|I_{k+1})}{P(m|I_k)} - \sum_{m=1}^M P(m|I_N) \ln \frac{P(m|I_N)}{P(m|I_0)} \right] \\
&= \alpha_M \sum_{m=1}^M \mathbb{E}_{I_N|\pi, I_0} \left[ \sum_{k=0}^{N-1} P(m|I_{k+1}) \ln \frac{P(m|I_{k+1})}{P(m|I_k)} - P(m|I_N) \ln \frac{P(m|I_N)}{P(m|I_0)} \right] \\
&= \alpha_M \sum_{m=1}^M \mathbb{E}_{I_N|\pi, I_0} \left[ \sum_{k=0}^{N-2} P(m|I_{k+1}) \ln \frac{P(m|I_{k+1})}{P(m|I_k)} + P(m|I_N) \ln \frac{P(m|I_N)}{P(m|I_{N-1})} \right. \\
&\quad \left. - P(m|I_N) \ln \frac{P(m|I_N)}{P(m|I_0)} \right] \\
&= \alpha_M \sum_{m=1}^M \mathbb{E}_{I_N|\pi, I_0} \left[ \sum_{k=0}^{N-2} P(m|I_{k+1}) \ln \frac{P(m|I_{k+1})}{P(m|I_k)} - P(m|I_N) \ln \frac{P(m|I_{N-1})}{P(m|I_0)} \right] \\
&= \alpha_M \sum_{m=1}^M \mathbb{E}_{I_{N-1}|\pi, I_0} \left[ \sum_{k=0}^{N-2} P(m|I_{k+1}) \ln \frac{P(m|I_{k+1})}{P(m|I_k)} - \mathbb{E}_{I_N|\pi, I_{N-1}} P(m|I_N) \ln \frac{P(m|I_{N-1})}{P(m|I_0)} \right] \\
&= \alpha_M \sum_{m=1}^M \mathbb{E}_{I_{N-1}|\pi, I_0} \left[ \sum_{k=0}^{N-2} P(m|I_{k+1}) \ln \frac{P(m|I_{k+1})}{P(m|I_k)} - P(m|I_{N-1}) \ln \frac{P(m|I_{N-1})}{P(m|I_0)} \right] \\
&\quad \vdots \\
&= \alpha_M \sum_{m=1}^M \mathbb{E}_{I_1|\pi, I_0} \left[ \sum_{k=0}^0 P(m|I_{k+1}) \ln \frac{P(m|I_{k+1})}{P(m|I_k)} - P(m|I_1) \ln \frac{P(m|I_1)}{P(m|I_0)} \right] \\
&= 0,
\end{aligned}$$

where the seventh equality is due to

$$\begin{aligned}
\mathbb{E}_{I_N|\pi, I_{N-1}} P(m|I_N) \ln \frac{P(m|I_{N-1})}{P(m|I_0)} &= \int_{\mathcal{Y}} p(y_{N-1}|\pi, I_{N-1}) P(m|I_N) \ln \frac{P(m|I_{N-1})}{P(m|I_0)} dy_{N-1} \\
&= \int_{\mathcal{Y}} p(y_{N-1}, m|\pi, I_{N-1}) \ln \frac{P(m|I_{N-1})}{P(m|I_0)} dy_{N-1} \\
&= P(m|I_{N-1}) \ln \frac{P(m|I_{N-1})}{P(m|I_0)}
\end{aligned}$$

with  $P(m|I_N) = P(m|I_{N-1}, \pi, y_{N-1})$  since the policy is deterministic, and the eighth equality results from repeatedly applying the steps between the third and seventh equalities until  $N = 1$ .

For the part corresponding to IG on the PoIs:

$$\begin{aligned}
& U_I(\pi; \alpha_\Theta) - U_T(\pi; \alpha_\Theta) \\
&= \alpha_\Theta \mathbb{E}_{I_N|\pi, I_0} \left[ \sum_{k=0}^{N-1} \mathbb{E}_{m|I_{k+1}} D_{\text{KL}}(p(\theta_m|I_{k+1}) || p(\theta_m|I_k)) - \mathbb{E}_{m|I_N} D_{\text{KL}}(p(\theta_m|I_N) || p(\theta_m|I_0)) \right] \\
&= \alpha_\Theta \sum_{m=1}^M \mathbb{E}_{I_N|\pi, I_0} \left[ \sum_{k=0}^{N-1} P(m|I_{k+1}) D_{\text{KL}}(p(\theta_m|I_{k+1}) || p(\theta_m|I_k)) \right. \\
&\quad \left. - P(m|I_N) D_{\text{KL}}(p(\theta_m|I_N) || p(\theta_m|I_0)) \right] \\
&= \alpha_\Theta \sum_{m=1}^M \mathbb{E}_{I_N|\pi, I_0} \left[ \sum_{k=0}^{N-2} P(m|I_{k+1}) D_{\text{KL}}(p(\theta_m|I_{k+1}) || p(\theta_m|I_k)) \right. \\
&\quad \left. + P(m|I_N) D_{\text{KL}}(p(\theta_m|I_N) || p(\theta_m|I_{N-1})) \right. \\
&\quad \left. - P(m|I_N) D_{\text{KL}}(p(\theta_m|I_N) || p(\theta_m|I_0)) \right] \\
&= \alpha_\Theta \sum_{m=1}^M \mathbb{E}_{I_N|\pi, I_0} \left[ \sum_{k=0}^{N-2} P(m|I_{k+1}) D_{\text{KL}}(p(\theta_m|I_{k+1}) || p(\theta_m|I_k)) \right. \\
&\quad \left. + P(m|I_N) \int_{\Theta} p(\theta_m|I_N) \ln \frac{p(\theta_m|I_0)}{p(\theta_m|I_{N-1})} d\theta_m \right] \\
&= \alpha_\Theta \sum_{m=1}^M \mathbb{E}_{I_{N-1}|\pi, I_0} \left[ \sum_{k=0}^{N-2} P(m|I_{k+1}) D_{\text{KL}}(p(\theta_m|I_{k+1}) || p(\theta_m|I_k)) \right. \\
&\quad \left. + \mathbb{E}_{I_N|\pi, I_{N-1}} P(m|I_N) \int_{\Theta} p(\theta_m|I_N) \ln \frac{p(\theta_m|I_0)}{p(\theta_m|I_{N-1})} d\theta_m \right] \\
&= \alpha_\Theta \sum_{m=1}^M \mathbb{E}_{I_{N-1}|\pi, I_0} \left[ \sum_{k=0}^{N-2} P(m|I_{k+1}) D_{\text{KL}}(p(\theta_m|I_{k+1}) || p(\theta_m|I_k)) \right. \\
&\quad \left. - P(m|I_{N-1}) D_{\text{KL}}(p(\theta_m|I_{N-1}) || p(\theta_m|I_0)) \right] \\
&\quad \vdots \\
&= \alpha_\Theta \sum_{m=1}^M \mathbb{E}_{I_1|\pi, I_0} \left[ \sum_{k=0}^0 P(m|I_{k+1}) D_{\text{KL}}(p(\theta_m|I_{k+1}) || p(\theta_m|I_k)) \right. \\
&\quad \left. - P(m|I_1) D_{\text{KL}}(p(\theta_m|I_1) || p(\theta_m|I_0)) \right] \\
&= 0,
\end{aligned}$$

where the fourth equality is due to

$$\begin{aligned}
& P(m|I_N) D_{\text{KL}}(p(\theta_m|I_N) || p(\theta_m|I_{N-1})) - P(m|I_N) D_{\text{KL}}(p(\theta_m|I_N) || p(\theta_m|I_0)) \\
&= P(m|I_N) \int_{\Theta} p(\theta_m|I_N) \left[ \ln \frac{p(\theta_m|I_N)}{p(\theta_m|I_{N-1})} - \ln \frac{p(\theta_m|I_N)}{p(\theta_m|I_0)} \right] d\theta_m \\
&= P(m|I_N) \int_{\Theta} p(\theta_m|I_N) \ln \frac{p(\theta_m|I_0)}{p(\theta_m|I_{N-1})} d\theta_m,
\end{aligned}$$

and the sixth equality is due to

$$\begin{aligned}
& \mathbb{E}_{I_N|\pi, I_{N-1}} P(m|I_N) \int_{\Theta} p(\theta_m|I_N) \ln \frac{p(\theta_m|I_0)}{p(\theta_m|I_{N-1})} d\theta_m \\
&= \int_{\mathcal{Y}} P(y_{N-1}|\pi, I_{N-1}) P(m|I_N) \int_{\Theta} p(\theta_m|I_N) \ln \frac{p(\theta_m|I_0)}{p(\theta_m|I_{N-1})} d\theta_m dy_{N-1} \\
&= \int_{\mathcal{Y}} \int_{\Theta} P(y_{N-1}, m, \theta_m|\pi, I_{N-1}) \ln \frac{p(\theta_m|I_0)}{p(\theta_m|I_{N-1})} d\theta_m dy_{N-1} \\
&= P(m|I_{N-1}) \int_{\Theta} P(\theta_m|I_{N-1}) \ln \frac{p(\theta_m|I_0)}{p(\theta_m|I_{N-1})} d\theta_m dy_{N-1} \\
&= -P(m|I_{N-1}) D_{\text{KL}}(p(\theta_m|I_{N-1}) || p(\theta_m|I_0)),
\end{aligned}$$

and the seventh equality results from repeatedly applying the steps between the second and sixth equalities until  $N = 1$ .

For the part corresponding to IG on the QoIs, the derivation is identical as above for the PoIs except replacing  $\theta_m$  with  $z_m$ , to arrive at

$$U_I(\pi; \alpha_Z) - U_T(\pi; \alpha_Z) = 0.$$

Combining the equivalence results from the four parts, we obtain

$$U_I(\pi) = U_T(\pi)$$

for any policy  $\pi$ . □

#### A.4 Proof of Theorem 2 (One-point-estimate equivalence)

*Proof.* We begin by proving the equivalence of expected utility under the TIG and one-point-TIG:

$$\begin{aligned}
U_T(\pi) &= \mathbb{E}_{I_N|\pi, I_0} \left[ \sum_{k=0}^{N-1} g_k(I_k, d_k, y_k) + g_N(I_N) \right] \\
&= \mathbb{E}_{I_N|\pi, I_0} \left[ \alpha_M D_{\text{KL}}(P(m|I_N) || P(m)) \right. \\
&\quad \left. + \mathbb{E}_{m|I_N} [\alpha_\Theta D_{\text{KL}}(p(\theta_m|I_N) || p(\theta_m)) + \alpha_Z D_{\text{KL}}(p(z_m|I_N) || p(z_m))] \right] \\
&= \mathbb{E}_{I_N|\pi, I_0} \left[ \alpha_M \mathbb{E}_{m|I_N} \ln \frac{P(m|I_N)}{P(m)} \right. \\
&\quad \left. + \mathbb{E}_{m|I_N} \left[ \alpha_\Theta \mathbb{E}_{\theta_m|I_N} \ln \frac{p(\theta_m|I_N)}{p(\theta_m)} + \alpha_Z \mathbb{E}_{z_m|I_N} \ln \frac{p(z_m|I_N)}{p(z_m)} \right] \right] \\
&= \mathbb{E}_{m, I_N|\pi, I_0} \left[ \alpha_M \ln \frac{P(m|I_N)}{P(m)} \right. \\
&\quad \left. + \alpha_\Theta \mathbb{E}_{\theta_m|I_N} \ln \frac{p(\theta_m|I_N)}{p(\theta_m)} + \alpha_Z \mathbb{E}_{z_m|I_N} \ln \frac{p(z_m|I_N)}{p(z_m)} \right] \\
&= \mathbb{E}_{m, I_N|\pi, I_0} \left[ \alpha_M \mathbb{E}_{\theta_m, z_m|I_N} \ln \frac{P(m|I_N)}{P(m)} \right. \\
&\quad \left. + \alpha_\Theta \mathbb{E}_{\theta_m, z_m|I_N} \ln \frac{p(\theta_m|I_N)}{p(\theta_m)} + \alpha_Z \mathbb{E}_{\theta_m, z_m|I_N} \ln \frac{p(z_m|I_N)}{p(z_m)} \right] \\
&= \mathbb{E}_{m, \theta_m, z_m, I_N|\pi, I_0} \left[ \alpha_M \ln \frac{P(m|I_N)}{P(m)} + \alpha_\Theta \ln \frac{p(\theta_m|I_N)}{p(\theta_m)} + \alpha_Z \ln \frac{p(z_m|I_N)}{p(z_m)} \right] \\
&= \mathbb{E}_{m, \theta_m, \eta_m, z_m, I_N|\pi, I_0} \left[ \alpha_M \ln \frac{P(m|I_N)}{P(m)} + \alpha_\Theta \ln \frac{p(\theta_m|I_N)}{p(\theta_m)} + \alpha_Z \ln \frac{p(z_m|I_N)}{p(z_m)} \right] \\
&= \mathbb{E}_{\dot{m}, \dot{\theta}_m, \dot{\eta}_m, \dot{z}_m} \mathbb{E}_{I_N|\pi, I_0, \dot{m}, \dot{\theta}_m, \dot{\eta}_m} \left[ \alpha_M \ln \frac{P(\dot{m}|I_N)}{P(\dot{m})} + \alpha_\Theta \ln \frac{p(\dot{\theta}_m|I_N)}{p(\dot{\theta}_m)} + \alpha_Z \ln \frac{p(\dot{z}_m|I_N)}{p(\dot{z}_m)} \right] \\
&= \dot{U}_T(\pi).
\end{aligned}$$

Next, we have already established the equivalence  $U_T(\pi) = U_I(\pi)$  in Appendix A.3. Finally, we show the equivalence between  $\dot{U}_I(\pi)$  and  $\dot{U}_T(\pi)$  by cancelling out all intermediate posteriors:

$$\begin{aligned}
\dot{U}_I(\pi) &= \mathbb{E}_{\dot{m}, \dot{\theta}_m, \dot{\eta}_m, \dot{z}_m} \mathbb{E}_{I_N|\pi, I_0, \dot{m}, \dot{\theta}_m, \dot{\eta}_m} \sum_{k=0}^{N-1} \left[ \alpha_M \ln \frac{P(\dot{m}|I_{k+1})}{P(\dot{m}|I_k)} + \alpha_\Theta \ln \frac{p(\dot{\theta}_m|I_{k+1})}{p(\dot{\theta}_m|I_k)} + \alpha_Z \ln \frac{p(\dot{z}_m|I_{k+1})}{p(\dot{z}_m|I_k)} \right] \\
&\tag{19}
\end{aligned}$$

$$\begin{aligned}
&= \mathbb{E}_{\dot{m}, \dot{\theta}_m, \dot{\eta}_m, \dot{z}_m} \mathbb{E}_{I_N|\pi, I_0, \dot{m}, \dot{\theta}_m, \dot{\eta}_m} \left[ \alpha_M \ln \frac{P(\dot{m}|I_N)}{P(\dot{m})} + \alpha_\Theta \ln \frac{p(\dot{\theta}_m|I_N)}{p(\dot{\theta}_m)} + \alpha_Z \ln \frac{p(\dot{z}_m|I_N)}{p(\dot{z}_m)} \right] \\
&\tag{20}
\end{aligned}$$

$$= \dot{U}_T(\pi).$$

Combining the above equivalence results together, we have

$$U_T(\pi) = \dot{U}_T(\pi) = \dot{U}_I(\pi) = U_I(\pi)$$

for any policy  $\pi$ . □

## A.5 Omitting prior terms

The difference between the expected utilities under the one-point IG estimate formulations that omit and include the prior term is:

$$\begin{aligned}
 \delta \dot{U}(\pi) &= \mathbb{E}_{\dot{r}_m, \dot{\theta}_m, \dot{\eta}_m, \dot{z}_m} \mathbb{E}_{I_N | \pi, I_0, \dot{r}_m, \dot{\theta}_m, \dot{\eta}_m} \left[ \alpha_M \ln P(\dot{r}_m) + \alpha_\Theta \ln p(\dot{\theta}_m) + \alpha_Z \ln p(\dot{z}_m) \right] \\
 &= \mathbb{E}_{\dot{r}_m, \dot{\theta}_m, \dot{\eta}_m, \dot{z}_m} \left[ \alpha_M \ln P(\dot{r}_m) + \alpha_\Theta \ln p(\dot{\theta}_m) + \alpha_Z \ln p(\dot{z}_m) \right],
 \end{aligned}$$

which is constant with respect to the policy  $\pi$ . Therefore, whether including or omitting the prior terms will not affect the optimal policy (i.e. the arg-max to the expected utilities). The same conclusion can be drawn for the expected utilities under the full IG formulations.

## A.6 Proof of Theorem 3 (Variational lower bound)

*Proof.* Appendix A.7 shows that the expected utilities using the variational-one-point-TIG and variational-one-point-IIG are equivalent. Thus, below we prove the lower bound under the variational-one-point-TIG, and the same result carries over to the variational-one-point-IIG due to their equivalence.

The difference between the expected utility and the variational expected utility is

$$\begin{aligned}
& \dot{U}(\pi) - \dot{U}(\pi; \phi) \\
&= \mathbb{E}_{\dot{m}, \dot{\theta}_m, \dot{\eta}_m, \dot{z}_m} \mathbb{E}_{I_N | \pi, I_0, \dot{m}, \dot{\theta}_m, \dot{\eta}_m} \left[ \alpha_M \ln \frac{P(\dot{m} | I_N)}{q(\dot{m} | I_N; \phi_M)} + \alpha_\Theta \ln \frac{p(\dot{\theta}_m | I_N)}{q(\dot{\theta}_m | I_N; \phi_{\Theta_m})} \right. \\
&\quad \left. + \alpha_Z \ln \frac{p(\dot{z}_m | I_N)}{q(\dot{z}_m | I_N; \phi_{Z_m})} \right] \\
&= \alpha_M \mathbb{E}_{\dot{m}, \dot{\theta}_m, \dot{\eta}_m, \dot{z}_m} \mathbb{E}_{I_N | \pi, I_0, \dot{m}, \dot{\theta}_m, \dot{\eta}_m} \left[ \ln \frac{P(\dot{m} | I_N)}{q(\dot{m} | I_N; \phi_M)} \right] \\
&\quad + \alpha_\Theta \mathbb{E}_{\dot{m}, \dot{\theta}_m, \dot{\eta}_m, \dot{z}_m} \mathbb{E}_{I_N | \pi, I_0, \dot{m}, \dot{\theta}_m, \dot{\eta}_m} \left[ \ln \frac{p(\dot{\theta}_m | I_N)}{q(\dot{\theta}_m | I_N; \phi_{\Theta_m})} \right] \\
&\quad + \alpha_Z \mathbb{E}_{\dot{m}, \dot{\theta}_m, \dot{\eta}_m, \dot{z}_m} \mathbb{E}_{I_N | \pi, I_0, \dot{m}, \dot{\theta}_m, \dot{\eta}_m} \left[ \ln \frac{p(\dot{z}_m | I_N)}{q(\dot{z}_m | I_N; \phi_{Z_m})} \right] \\
&= \alpha_M \mathbb{E}_{\dot{m}, \dot{\theta}_m, \dot{\eta}_m, \dot{z}_m, I_N | \pi, I_0} \left[ \ln \frac{P(\dot{m} | I_N)}{q(\dot{m} | I_N; \phi_M)} \right] \\
&\quad + \alpha_\Theta \mathbb{E}_{\dot{m}, \dot{\theta}_m, \dot{\eta}_m, \dot{z}_m, I_N | \pi, I_0} \left[ \ln \frac{p(\dot{\theta}_m | I_N)}{q(\dot{\theta}_m | I_N; \phi_{\Theta_m})} \right] \\
&\quad + \alpha_Z \mathbb{E}_{\dot{m}, \dot{\theta}_m, \dot{\eta}_m, \dot{z}_m, I_N | \pi, I_0} \left[ \ln \frac{p(\dot{z}_m | I_N)}{q(\dot{z}_m | I_N; \phi_{Z_m})} \right] \\
&= \alpha_M \mathbb{E}_{\dot{m}, I_N | \pi, I_0} \left[ \ln \frac{P(\dot{m} | I_N)}{q(\dot{m} | I_N; \phi_M)} \right] \\
&\quad + \alpha_\Theta \mathbb{E}_{\dot{m}, \dot{\theta}_m, I_N | \pi, I_0} \left[ \ln \frac{p(\dot{\theta}_m | I_N)}{q(\dot{\theta}_m | I_N; \phi_{\Theta_m})} \right] \\
&\quad + \alpha_Z \mathbb{E}_{\dot{m}, \dot{z}_m, I_N | \pi, I_0} \left[ \ln \frac{p(\dot{z}_m | I_N)}{q(\dot{z}_m | I_N; \phi_{Z_m})} \right] \\
&= \alpha_M \mathbb{E}_{I_N | \pi, I_0} \mathbb{E}^{\dot{m} | I_N} \left[ \ln \frac{P(\dot{m} | I_N)}{q(\dot{m} | I_N; \phi_M)} \right] \\
&\quad + \alpha_\Theta \mathbb{E}_{\dot{m}, I_N | \pi, I_0} \mathbb{E}^{\dot{\theta}_m | \dot{m}, I_N} \left[ \ln \frac{p(\dot{\theta}_m | I_N)}{q(\dot{\theta}_m | I_N; \phi_{\Theta_m})} \right] \\
&\quad + \alpha_Z \mathbb{E}_{\dot{m}, I_N | \pi, I_0} \mathbb{E}^{\dot{z}_m | \dot{m}, I_N} \left[ \ln \frac{p(\dot{z}_m | I_N)}{q(\dot{z}_m | I_N; \phi_{Z_m})} \right] \\
&= \alpha_M \mathbb{E}_{I_N | \pi, I_0} \left[ D_{\text{KL}}(P(\dot{m} | I_N) || q(\dot{m} | I_N; \phi_M)) \right] \\
&\quad + \alpha_\Theta \mathbb{E}_{\dot{m}, I_N | \pi, I_0} \left[ D_{\text{KL}}(p(\dot{\theta}_m | I_N) || q(\dot{\theta}_m | I_N; \phi_{\Theta_m})) \right] \\
&\quad + \alpha_Z \mathbb{E}_{\dot{m}, I_N | \pi, I_0} \left[ D_{\text{KL}}(p(\dot{z}_m | I_N) || q(\dot{z}_m | I_N; \phi_{Z_m})) \right] \\
&\geq 0
\end{aligned}$$

where  $\alpha_M \geq 0$ ,  $\alpha_\Theta \geq 0$ ,  $\alpha_Z \geq 0$ . The sixth equality is due to  $p(\dot{\theta}_m | I_N)$  being equivalent to  $p(\dot{\theta}_m | \dot{m}, I_N)$  and  $p(\dot{z}_m | I_N)$  being equivalent to  $p(\dot{z}_m | \dot{m}, I_N)$ , due to the notation convention

adopted in this paper. The bound is tight if and only if  $q(\cdot|I_N; \phi(\cdot)) = p(\cdot|I_N)$  (except the trivial case when  $\alpha_M = \alpha_\Theta = \alpha_Z = 0$ ).

□

## A.7 Cancellation of intermediate posteriors

Similar to Eqn. (19) and Eqn. (20), all intermediate variational posteriors  $q(\cdot|I_k; \phi(\cdot))$  for  $k = 1, \dots, N-1$  cancel out:

$$\begin{aligned}
& \dot{U}_I(\pi; \phi) \\
&= \mathbb{E}_{\dot{m}, \dot{\theta}_m, \dot{\eta}_m, \dot{z}_m} \mathbb{E}_{I_N | \pi, I_0, \dot{m}, \dot{\theta}_m, \dot{\eta}_m} \sum_{k=0}^{N-1} \left[ \alpha_M \ln \frac{q(\dot{m}|I_{k+1}; \phi_M)}{q(\dot{m}|I_k; \phi_M)} \right. \\
&\quad \left. + \alpha_\Theta \ln \frac{q(\dot{\theta}_m|I_{k+1}; \phi_{\Theta_m})}{q(\dot{\theta}_m|I_k; \phi_{\Theta_m})} + \alpha_Z \ln \frac{q(\dot{z}_m|I_{k+1}; \phi_{Z_m})}{q(\dot{z}_m|I_k; \phi_{Z_m})} \right] \\
&= \mathbb{E}_{\dot{m}, \dot{\theta}_m, \dot{\eta}_m, \dot{z}_m} \mathbb{E}_{I_N | \pi, I_0, \dot{m}, \dot{\theta}_m, \dot{\eta}_m} \left[ \right. \\
&\quad \alpha_M \left( \ln \frac{q(\dot{m}|I_1; \phi_M)}{P(\dot{m})} + \ln \frac{q(\dot{m}|I_2; \phi_M)}{q(\dot{m}|I_1; \phi_M)} + \dots + \ln \frac{q(\dot{m}|I_N; \phi_M)}{q(\dot{m}|I_{N-1}; \phi_M)} \right) \\
&\quad + \alpha_\Theta \left( \ln \frac{q(\dot{\theta}_m|I_1; \phi_{\Theta_m})}{p(\dot{\theta}_m)} + \ln \frac{q(\dot{\theta}_m|I_2; \phi_{\Theta_m})}{q(\dot{\theta}_m|I_1; \phi_{\Theta_m})} + \dots + \ln \frac{q(\dot{\theta}_m|I_N; \phi_{\Theta_m})}{q(\dot{\theta}_m|I_{N-1}; \phi_{\Theta_m})} \right) \\
&\quad \left. + \alpha_Z \left( \ln \frac{q(\dot{z}_m|I_1; \phi_{Z_m})}{p(\dot{z}_m)} + \ln \frac{q(\dot{z}_m|I_2; \phi_{Z_m})}{q(\dot{z}_m|I_1; \phi_{Z_m})} + \dots + \ln \frac{q(\dot{z}_m|I_N; \phi_{Z_m})}{q(\dot{z}_m|I_{N-1}; \phi_{Z_m})} \right) \right] \\
&= \mathbb{E}_{\dot{m}, \dot{\theta}_m, \dot{\eta}_m, \dot{z}_m} \mathbb{E}_{I_N | \pi, I_0, \dot{m}, \dot{\theta}_m, \dot{\eta}_m} \left[ \alpha_M \ln \frac{q(\dot{m}|I_N; \phi_M)}{P(\dot{m})} \right. \\
&\quad \left. + \alpha_\Theta \ln \frac{q(\dot{\theta}_m|I_N; \phi_{\Theta_m})}{p(\dot{\theta}_m)} + \alpha_Z \ln \frac{q(\dot{z}_m|I_N; \phi_{Z_m})}{p(\dot{z}_m)} \right] \\
&= \dot{U}_T(\pi; \phi).
\end{aligned}$$

Therefore, only the prior and the final variational posterior terms contribute to the variational expected utility. Since the prior PDF is either known or omitted, the accuracy of the variational expected utility only depends on the quality of the final variational posterior approximation.

## B Algorithm details

### B.1 Neural network architecture of model posterior predictor

The overall architecture of a neural network (NN)-based posterior predictor for model probability ( $q(m|I_k; \phi_M)$ ) is shown in Table 1; the same architecture is utilized for all numerical cases in this work. More specifically, the model posterior predictor takes  $I_k$  as input, and outputs the log-probabilities of each candidate model  $\ln q(m|I_k; \phi_M)$ . Separate model posterior predictors are trained for each stage when the IIG formulation is used. However, as shown earlier in Appendix A.7, the quality of the intermediate variational posterior approximations does not directly contribute to the accuracy of the overall variational expected utility estimate, and thus one may elect to train these intermediate model posterior predictors more “loosely”, for example, by using smaller NN architectures and with shared weights among the NNs.

### B.2 Neural network architectures of parameter and predictive quantity posterior predictors

We introduce the Gaussian Mixture Models (GMMs) and normalizing flow (NF)-based posterior predictors for PoIs ( $q(\theta_m|I_k; \phi_{\Theta_m})$ ) and QoIs ( $q(z_m|I_k; \phi_{Z_m})$ ). We adopt the same architectures for

Table 1: Architecture of the NN-based model posterior predictor.

Layer	Description	Dimension	Activation
Input	$I_k$	$k(N_d + N_y)$	-
H1	Dense	256	ReLU
H2	Dense	256	ReLU
H3	Dense	256	ReLU
Output	Dense	$M$	LogSoftmax

both the PoI and QoI posterior predictors, and so only introduce them in the context of PoIs below but with the understanding that the same applies to the QoIs. Similar to the model posterior predictor, separate PoI and QoI posterior predictors are trained for each stage when the IIG formulation is used.

### B.2.1 Independent Gaussian Mixture Models

An independent GMM approximates a complex distribution through a weighted sum of multiple independent Gaussians:

$$q(\theta_m | I_k; \phi_{\Theta_m}) = \sum_{i=1}^{n_{\text{mixture}}} w_i(I_k; \phi_{\Theta_m}) \mathcal{N}(\theta_m; \mu_i(I_k; \phi_{\Theta_m}), \Sigma_i(I_k; \phi_{\Theta_m})), \quad (21)$$

where for the  $i$ th Gaussian,  $w_i(I_k; \phi_{\Theta_m})$  is its mixture weight,  $\mu_i(I_k; \phi_{\Theta_m}) \in \mathbb{R}^{N_{\theta_m}}$  is its mean, and  $\Sigma_i(I_k; \phi_{\Theta_m}) \in \mathbb{R}^{N_{\theta_m} \times N_{\theta_m}}$  is its diagonal covariance matrix with the square root of the diagonal terms being the standard deviations. The weights, means, and standard deviations of the GMM are predicted using NNs, together referred to as the GMM net. These NNs share a common backend network that learns shared features. The architectures of the feature net, weight net, mean net and standard deviation net are provided in Table 2 to 4. The *Linear mapping* in Table 4 refers to the process of mapping the output to a specific range that is problem dependent. This mapping ensures that the predicted means and standard deviations of the GMM fall within the desired range. Additionally, an epsilon of  $10^{-27}$  is added to Eqn. (21) to prevent numerical underflow. When some PoIs have compact support, independent truncated normal distributions [7] are used to replace the dimensions corresponding to those PoIs within the Gaussian distributions. The specific ranges of the linear mapping and the usage of truncated normal will be mentioned in each numerical case. The same GMM net architecture is used across all numerical cases.

Table 2: Architecture of the feature net of the GMM net.

Layer	Description	Dimension	Activation
Input	$I_k$	$k(N_d + N_y)$	-
H1	Dense	256	ReLU
Output	Dense	256	ReLU

Table 3: Architecture of the weight net of the GMM net.

Layer	Description	Dimension	Activation
Input	Feature( $I_k$ )	256	-
H1	Dense	256	ReLU
H2	Dense	256	ReLU
Output	Dense	$n_{\text{mixture}}$	Softmax

### B.2.2 Normalizing Flows

A NF approximates a target random variable  $\theta$  by finding an overall invertible mapping to this target from a standard normal of the same dimension,  $\theta = g(\xi)$  (and  $\xi = f(\theta)$  where  $f = g^{-1}$ ), via a composition of successive invertible mappings. The PDFs of these random variables are related via

$$p_{\Theta}(\theta) = p_{\xi}(f(\theta)) |\det Df(\theta)| \quad (22)$$

Table 4: Architecture of the mean net or standard deviation net of the GMM net.

Layer	Description	Dimension	Activation
Input	Feature( $I_k$ )	256	-
H1	Dense	256	ReLU
H2	Dense	256	ReLU
H3	Dense	$n_{\text{mixture}}N_{\theta_m}$	Sigmoid
Output	Identity	$n_{\text{mixture}}N_{\theta_m}$	Linear mapping

where  $Df(\theta)$  is the Jacobian of  $f$  at  $\theta$ . Writing in a successive mapping form  $\theta = g(\xi) = g_n \circ g_{n-1} \circ \dots \circ g_1(\xi) = g_n(g_{n-1}(\dots(g_1(\xi))\dots))$  with  $n \geq 1$  invertible transformations, the log density is

$$\ln p_{\Theta}(\theta) = \ln p_{\xi}(f_n \circ f_{n-1} \circ \dots \circ f_1(\theta)) + \sum_{i=1}^n \ln |\det Df_i \circ f_{i-1} \circ \dots \circ f_1(\theta)| \quad (23)$$

where  $f(\theta) = f_n \circ f_{n-1} \circ \dots \circ f_1(\theta)$  and  $f_i = g_i^{-1}$ . The successive transformations on  $\xi$  can achieve a highly expressive density for the target variable  $\theta$  [13].

To approximate the PoI posterior  $q(\theta_m | I_k; \phi_{\Theta_m})$ , we build NF  $\xi = f(\theta)$  using an invertible neural network (INN) [13], and refer to the overall mapping as the NF net. INN partitions  $\theta$  into two parts  $\theta = [\theta_1, \theta_2]^T$  with approximately equal dimensions, and introduces invertible mappings

$$\begin{aligned} f_1(\theta) &= \begin{pmatrix} \theta_1 \\ \tilde{\theta}_2 = \theta_2 \odot \exp(s_1(\theta_1)) + t_1(\theta_1) \end{pmatrix} \\ f_2(f_1(\theta)) &= \begin{pmatrix} \tilde{\theta}_1 = \theta_1 \odot \exp(s_2(\tilde{\theta}_2)) + t_2(\tilde{\theta}_2) \\ \tilde{\theta}_2 \end{pmatrix} \end{aligned} \quad (24)$$

where  $s_1, t_1$  map  $\mathbb{R}^{n_{\theta_1}} \mapsto \mathbb{R}^{n_{\theta_2}}$  and  $s_2, t_2$  map  $\mathbb{R}^{n_{\theta_2}} \mapsto \mathbb{R}^{n_{\theta_1}}$ , and  $\odot$  denotes element-wise product. The Jacobian of  $f_1$  is

$$\begin{bmatrix} \mathbb{I}_d & 0 \\ \frac{\partial f_1(\theta)}{\partial \theta_2} & \text{diag}(\exp[s_1(\theta_1)]) \end{bmatrix},$$

a lower triangular matrix with determinant  $\exp[\sum_{j=1}^{n_{\theta_2}} s_1(\theta_1)_j]$ . Similarly the Jacobian of  $f_2$  is an upper triangular matrix with determinant  $\exp[\sum_{j=1}^{n_{\theta_1}} s_2(\tilde{\theta}_2)_j]$ .  $s$ 's and  $t$ 's can be represented via, for example, NNs for their expressiveness. Multiple such transformations from Eqn. (24) can also be composed together to further increase expressiveness of the overall mapping; we use  $n_{\text{trans}}$  to denote the number of such transformation.

To incorporate the dependency of posterior on  $I_k$ , the  $s(\cdot)$  and  $t(\cdot)$  are set up to also take  $I_k$  as input. Similar to the GMM setup,  $I_k$  is first fed into a feature network whose output has the same dimension as  $I_k$ . The architectures of the feature network, and the  $s_1, t_1; s_2, t_2$  networks in NFs are provided in Table 5 to 7. Mirroring the GMM net, an epsilon of  $10^{-27}$  is added to Eqn. (23) to prevent numerical underflow.

Table 5: Architecture of the feature net of the NF net. The first value under *Dimension* column is used for the source location problem in 6.1 and CES problem in C.5; the second value is used for the SIR problem in 6.2.

Layer	Description	Dimension	Activation
Input	$I_k$	$k(N_d + N_y)$	-
H1	Dense	256 / 128	ReLU
H2	Dense	256 / 128	ReLU
H3	Dense	256 / None	ReLU
Output	Feature( $I_k$ )	$k(N_d + N_y)$	-

### B.3 Neural network structure of actor and critic

The architectures of the actor and critic networks from [50] are adopted in this work. The actor  $\mu_{k,w}$  learns a mapping from state  $I_k$  to design  $d_k$ . Instead of learning separate actors for each stage, we

Table 6: Architecture of the  $s_1$  and  $t_1$  nets of the NF net. The first value under *Dimension* column is used for the source location problem in 6.1 and CES problem in C.5; the second value is used for the SIR problem in 6.2.

Layer	Description	Dimension	Activation
Input	Feature( $I_k$ ) + $\theta_1$	$k(N_d + N_y) + n_{\theta_1}$	-
H1	Dense	256 / 128	ReLU
H2	Dense	256 / 128	ReLU
H3	Dense	256 / 128	ReLU
Output	$s_1(\cdot)$ or $t_1(\cdot)$	$n_{\theta_2}$	-

Table 7: Architecture of the  $s_2$  and  $t_2$  nets of the NF net. The first value under *Dimension* column is used for the source location problem in 6.1 and CES problem in C.5; the second value is used for the SIR problem in 6.2.

Layer	Description	Dimension	Activation
Input	Feature( $I_k$ ) + $\tilde{\theta}_2$	$k(N_d + N_y) + n_{\theta_2}$	-
H1	Dense	256 / 128	ReLU
H2	Dense	256 / 128	ReLU
H3	Dense	256 / 128	ReLU
Output	$s_2(\cdot)$ or $t_2(\cdot)$	$n_{\theta_1}$	-

combine them into a single actor. The overall input takes the form

$$I_k^{actor} = [e_k, \tilde{I}_k]$$

where  $e_k$  is an 0-indexed one-hot encoding vector of size  $N$  to represent the current experiment stage:

$$e_k = [0, \dots, 0, \underbrace{1}_{k\text{th}}, 0, \dots, 0]^T,$$

and  $\tilde{I}_k$  is a vector of fixed size  $(N - 1)(N_d + N_y)$  obtained by extending  $I_k$  with zero-padding:

$$\tilde{I}_k = \left[ \overbrace{d_0, \dots, d_{k-1}}^{N_d}, \underbrace{0, \dots, 0}_{N_d(N-1-k)}, \overbrace{y_0, \dots, y_{k-1}}^{N_y}, \underbrace{0, \dots, 0}_{N_y(N-1-k)} \right]^T.$$

The total dimension of  $I_k^{actor}$  is  $N + (N - 1)(N_d + N_y)$ . The inputs of the critic is

$$I_k^{critic} = [I_k^{actor}, d_k]$$

with total dimension  $N + (N - 1)(N_d + N_y) + N_d$ . The output of the critic is a scalar. We note that without the presence of  $e_k$ , it would not be possible for the actor or the critic to distinguish between scenarios such as: whether at stage  $k$ , or at a later stage but the designs and observations from stage  $k$  are zero (i.e. the padded values). The architectures of the actor and critic are presented in Table 8 and Table 9, where the *Linear mapping* in Table 8 maps the output value to be within the design bounds. The same actor and critic architectures are used across all numerical cases.

Table 8: Architecture of the actor.

Layer	Description	Dimension	Activation
Input	$I_k^{actor}$	$N + (N - 1)(N_d + N_y)$	-
H1	Dense	256	ReLU
H2	Dense	256	ReLU
H3	Dense	256	ReLU
H4	Dense	$N_d$	Sigmoid
Output	Identity	$N_d$	Linear mapping

Table 9: Architecture of the critic.

Layer	Description	Dimension	Activation
Input	$I_k^{critic}$	$N + (N - 1)(N_d + N_y) + N_d$	-
H1	Dense	256	ReLU
H2	Dense	256	ReLU
H3	Dense	256	ReLU
Output	Dense	1	-

Other architectures have been proposed for constructing the actor and critic networks, such as the *encoder-pooling-emitter* structure used in [19, 30, 5]. These architectures leverage a permutation invariance property that arises from the conditional independence of likelihoods. However, it is important to note that in our case, the conditional independence of likelihoods does not hold, even if the likelihood function does not depend on past experience (i.e. if  $p(y_k|m, \theta_m, \eta_m, d_k, I_k) = p(y_k|m, \theta_m, \eta_m, d_k)$ ). For instance, if the problem involves multiple models, the model posterior can be shown to be not permutation invariant:

$$\begin{aligned}
P(m|I_N) &\propto P(m) \prod_{k=0}^{N-1} \int_{\Theta, \mathcal{H}} p(y_k|m, \theta_m, \eta_m, d_k) p(\theta_m, \eta_m|m, I_k) d\theta_m d\eta_m \\
&= P(m) \prod_{k=0}^{N-1} p(y_k|m, I_k, d_k) \\
&\neq P(m) \prod_{k=0}^{N-1} p(y_k|m, d_k)
\end{aligned}$$

since in the middle equation, we see that the factored marginal likelihoods in our case depend on the entire history  $I_k$ . Even when the problem only involves a single model (i.e.  $M = 1$ ), the PoI posterior is not permutation invariant if nuisance parameters are present:

$$\begin{aligned}
p(\theta_m|I_N) &\propto p(\theta_m) \prod_{k=0}^{N-1} \int_{\mathcal{H}} p(y_k|m, \theta_m, \eta_m, d_k) p(\eta_m|m, \theta_m, I_k) d\eta_m \\
&= p(\theta_m) \prod_{k=0}^{N-1} p(y_k|m, \theta_m, I_k, d_k) \\
&\neq p(\theta_m) \prod_{k=0}^{N-1} p(y_k|m, \theta_m, d_k).
\end{aligned}$$

Therefore, the *encoder-pooling-emitter* is not applicable and not adopted in this work. [30] further proposed to use long short-term memory networks (LSTM) as the history encoder when conditional independence does not hold. However, similar to the *encoder-pooling-emitter*, the backpropagation time of the LSTM encoder increases quadratically with horizon  $N$ , and becomes expensive for larger values of  $N$ .

## B.4 Algorithm of PG-vsOED

### B.4.1 Training of the posterior approximation

Due to the cancellation of intermediate posteriors as shown in Appendix A.7, the variational gradient in Eqn. (17) only involves the gradient of the final variational posterior:

$$\begin{aligned}
\nabla_{\phi} \dot{U}(w; \phi) &= \mathbb{E}_{\dot{m}, \dot{\theta}_m, \dot{\eta}_m, \dot{z}_m} \mathbb{E}_{I_N | \pi, I_0, \dot{m}, \dot{\theta}_m, \dot{\eta}_m} \left[ \alpha_M \nabla_{\phi_M} \ln q(\dot{m}|I_N; \phi_M) \right. \\
&\quad \left. + \alpha_{\Theta} \nabla_{\phi_{\Theta_m}} \ln q(\dot{\theta}_m|I_N; \phi_{\Theta_m}) \right. \\
&\quad \left. + \alpha_Z \nabla_{\phi_{Z_m}} \ln q(\dot{z}_m|I_N; \phi_{Z_m}) \right].
\end{aligned}$$

A Monte Carlo (MC) estimate for the variational gradient is:

$$\begin{aligned} \nabla_{\phi} \dot{U}(w; \phi) \approx & \frac{1}{n_{\text{batch}}} \sum_{i=1}^{n_{\text{batch}}} \left[ \alpha_M \nabla_{\phi_M} \ln q(\dot{m}^{(i)} | I_N^{(i)}; \phi_M) \right. \\ & + \alpha_{\Theta} \nabla_{\phi_{\Theta_m}} \ln q(\dot{\theta}_m^{(i)} | I_N^{(i)}; \phi_{\Theta_m}) \\ & \left. + \alpha_Z \nabla_{\phi_{Z_m}} \ln q(\dot{z}_m^{(i)} | I_N^{(i)}; \phi_{Z_m}) \right], \end{aligned}$$

where  $\dot{m}^{(i)}, \dot{\theta}_m^{(i)}, \dot{\eta}_m^{(i)}, \dot{z}_m^{(i)} \sim p(m, \theta_m, \eta_m, z_m)$  and  $I_N^{(i)} \sim p(I_N | \dot{m}^{(i)}, \dot{\theta}_m^{(i)}, \dot{\eta}_m^{(i)}, \pi_w)$ , and the gradients can be obtained by, for example, PyTorch Autograd. In our implementation, we draw samples from a replay buffer in order to reduce computations and to enable off-policy learning.

If the IIG formulation is used, the intermediate variational posteriors can be trained in the same manner with their MC gradient estimates:

$$\begin{aligned} \frac{1}{n_{\text{batch}}} \sum_{i=1}^{n_{\text{batch}}} \left[ \alpha_M \nabla_{\phi_M} \ln q(\dot{m}^{(i)} | I_k^{(i)}; \phi_M) \right. \\ + \alpha_{\Theta} \nabla_{\phi_{\Theta_m}} \ln q(\dot{\theta}_m^{(i)} | I_k^{(i)}; \phi_{\Theta_m}) \\ \left. + \alpha_Z \nabla_{\phi_{Z_m}} \ln q(\dot{z}_m^{(i)} | I_k^{(i)}; \phi_{Z_m}) \right] \end{aligned}$$

for  $k = 1, \dots, N - 1$ . The optimization of the variational posterior approximation is carried out using Adam [32] for all numerical cases. Hyperparameter tuning will be discussed in Appendix B.4.5, and specific hyperparameter settings will be specified for each case.

The variational posterior approximation is updated first during each outer iteration in Algorithm 1.

#### B.4.2 More about the critic

The *action-value function* (i.e. *critic*)  $Q_k^{\pi_w}(I_k, d_k)$  quantifies the expected cumulative remaining reward for conducting the  $k$ th experiment at design  $d_k$  and state  $I_k$ , and thereafter following policy  $\pi_w$ . The critics formulated with the the one-point reward estimates using either the true posterior or variational posterior are respectively

$$\begin{aligned} Q_k^{\pi_w}(I_k, d_k) &= \mathbb{E}_{\dot{m}, \dot{\theta}_m, \dot{\eta}_m, \dot{z}_m | I_k} \mathbb{E}_{I_N | \pi_w, I_k, d_k, \dot{m}, \dot{\theta}_m, \dot{\eta}_m} \left[ \sum_{k=0}^{N-1} \dot{g}_k(I_k, d_k, y_k) + \dot{g}_N(I_N) \right] \\ Q_k^{\pi_w}(I_k, d_k; \phi) &= \mathbb{E}_{\dot{m}, \dot{\theta}_m, \dot{\eta}_m, \dot{z}_m | I_k} \mathbb{E}_{I_N | \pi_w, I_k, d_k, \dot{m}, \dot{\theta}_m, \dot{\eta}_m} \left[ \sum_{k=0}^{N-1} \dot{g}_k(I_k, d_k, y_k; \phi) + \dot{g}_N(I_N; \phi) \right]. \end{aligned}$$

Specifically, the critics under TIG take the form:

$$\begin{aligned} Q_{T,k}^{\pi_w}(I_k, d_k) &= \mathbb{E}_{\dot{m}, \dot{\theta}_m, \dot{\eta}_m, \dot{z}_m | I_k} \mathbb{E}_{I_N | \pi_w, I_k, d_k, \dot{m}, \dot{\theta}_m, \dot{\eta}_m} \left[ \right. \\ & \quad \left. \alpha_M \ln \frac{P(\dot{m} | I_N)}{P(\dot{m})} + \alpha_{\Theta} \ln \frac{p(\dot{\theta}_m | I_N)}{p(\dot{\theta}_m)} + \alpha_Z \ln \frac{p(\dot{z}_m | I_N)}{p(\dot{z}_m)} \right] \\ Q_{T,k}^{\pi_w}(I_k, d_k; \phi) &= \mathbb{E}_{\dot{m}, \dot{\theta}_m, \dot{\eta}_m, \dot{z}_m | I_k} \mathbb{E}_{I_N | \pi_w, I_k, d_k, \dot{m}, \dot{\theta}_m, \dot{\eta}_m} \left[ \right. \\ & \quad \left. \alpha_M \ln \frac{q(\dot{m} | I_N; \phi_M)}{P(\dot{m})} + \alpha_{\Theta} \ln \frac{q(\dot{\theta}_m | I_N; \phi_{\Theta_m})}{p(\dot{\theta}_m)} + \alpha_Z \ln \frac{q(\dot{z}_m | I_N; \phi_{Z_m})}{p(\dot{z}_m)} \right], \end{aligned}$$

and the critics under IIG take the form:

$$\begin{aligned}
Q_{I,k}^{\pi_w}(I_k, d_k) &= \mathbb{E}_{\dot{m}, \dot{\theta}_m, \dot{\eta}_m, \dot{z}_m | I_k} \mathbb{E}_{I_N | \pi_w, I_k, d_k, \dot{m}, \dot{\theta}_m, \dot{\eta}_m} \left[ \right. \\
&\quad \left. \alpha_M \ln \frac{P(\dot{m} | I_N)}{P(\dot{m} | I_k)} + \alpha_\Theta \ln \frac{p(\dot{\theta}_m | I_N)}{p(\dot{\theta}_m | I_k)} + \alpha_Z \ln \frac{p(\dot{z}_m | I_N)}{p(\dot{z}_m | I_k)} \right] \\
Q_{I,k}^{\pi_w}(I_k, d_k; \phi) &= \mathbb{E}_{\dot{m}, \dot{\theta}_m, \dot{\eta}_m, \dot{z}_m | I_k} \mathbb{E}_{I_N | \pi_w, I_k, d_k, \dot{m}, \dot{\theta}_m, \dot{\eta}_m} \left[ \right. \\
&\quad \left. \alpha_M \ln \frac{q(\dot{m} | I_N; \phi_M)}{q(\dot{m} | I_k; \phi_M)} + \alpha_\Theta \ln \frac{q(\dot{\theta}_m | I_N; \phi_{\Theta_m})}{q(\dot{\theta}_m | I_k; \phi_{\Theta_m})} + \alpha_Z \ln \frac{q(\dot{z}_m | I_N; \phi_{Z_m})}{q(\dot{z}_m | I_k; \phi_{Z_m})} \right].
\end{aligned}$$

**Remark 1:** The difference between the one-point-TIG and -IIG critics is

$$\begin{aligned}
Q_{T,k}^{\pi_w}(I_k, d_k) - Q_{I,k}^{\pi_w}(I_k, d_k) &= \mathbb{E}_{\dot{m}, \dot{\theta}_m, \dot{\eta}_m, \dot{z}_m | I_k} \mathbb{E}_{I_N | \pi_w, I_k, d_k, \dot{m}, \dot{\theta}_m, \dot{\eta}_m} \left[ \right. \\
&\quad \left. \alpha_M \ln \frac{P(\dot{m} | I_k)}{P(\dot{m})} + \alpha_\Theta \ln \frac{p(\dot{\theta}_m | I_k)}{p(\dot{\theta}_m)} + \alpha_Z \ln \frac{p(\dot{z}_m | I_k)}{p(\dot{z}_m)} \right] \\
&= \mathbb{E}_{\dot{m}, \dot{\theta}_m, \dot{\eta}_m, \dot{z}_m | I_k} \left[ \right. \\
&\quad \left. \alpha_M \ln \frac{P(\dot{m} | I_k)}{P(\dot{m})} + \alpha_\Theta \ln \frac{p(\dot{\theta}_m | I_k)}{p(\dot{\theta}_m)} + \alpha_Z \ln \frac{p(\dot{z}_m | I_k)}{p(\dot{z}_m)} \right],
\end{aligned}$$

which is constant with respect to  $d_k$ . Since  $\nabla_{d_k} Q_k^{\pi_w}(I_k, d_k)$  is used in the policy gradient (Eqn. (18)), then whether adopting  $Q_{T,k}^{\pi_w}(I_k, d_k)$  or  $Q_{I,k}^{\pi_w}(I_k, d_k)$  will result in the same policy gradient value.

**Remark 2:** The difference between  $Q_{T,k}^{\pi_w}(I_k, d_k)$  and  $Q_{T,k}^{\pi_w}(I_k, d_k; \phi)$  is

$$\begin{aligned}
&Q_{T,k}^{\pi_w}(I_k, d_k) - Q_{T,k}^{\pi_w}(I_k, d_k; \phi) \\
&= \mathbb{E}_{\dot{m}, \dot{\theta}_m, \dot{\eta}_m, \dot{z}_m | I_k} \mathbb{E}_{I_N | \pi_w, I_k, d_k, \dot{m}, \dot{\theta}_m, \dot{\eta}_m} \left[ \right. \\
&\quad \left. \alpha_M \ln \frac{P(\dot{m} | I_N)}{q(\dot{m} | I_N; \phi_M)} + \alpha_\Theta \ln \frac{p(\dot{\theta}_m | I_N)}{q(\dot{\theta}_m | I_N; \phi_{\Theta_m})} + \alpha_Z \ln \frac{p(\dot{z}_m | I_N)}{q(\dot{z}_m | I_N; \phi_{Z_m})} \right] \\
&= \mathbb{E}_{I_N | \pi_w, I_k, d_k} \left[ \alpha_M D_{\text{KL}}(P(m | I_N) || q(m | I_N; \phi_M)) \right. \\
&\quad \left. + \mathbb{E}_{m | I_N} [\alpha_\Theta D_{\text{KL}}(p(\theta_m | I_N) || q(\theta_m | I_N; \phi_{\Theta_m})) + \alpha_Z D_{\text{KL}}(p(z_m | I_N) || q(z_m | I_N; \phi_{Z_m}))] \right],
\end{aligned}$$

which is an expected weighted KL divergence (with positive weights). It equals to zero if and only if the variational posterior approximations  $q(\cdot | I_N; \phi_{(\cdot)})$  are equal to the true posteriors  $p(\cdot | I_N)$  (except the trivial case when  $\alpha_M = \alpha_\Theta = \alpha_Z = 0$ ). In other words,  $Q_{T,k}^{\pi_w}(I_k, d_k; \phi)$  forms a lower bound of  $Q_{T,k}^{\pi_w}(I_k, d_k)$ , and learning an accurate variational posterior approximation could also help reduce the bias in the critic.

**Remark 3:** The difference between  $Q_{I,k}^{\pi_w}(I_k, d_k)$  and  $Q_{I,k}^{\pi_w}(I_k, d_k; \phi)$  is

$$\begin{aligned}
& Q_{I,k}^{\pi_w}(I_k, d_k) - Q_{I,k}^{\pi_w}(I_k, d_k; \phi) \\
&= \mathbb{E}_{\dot{m}, \dot{\theta}_m, \dot{\eta}_m, \dot{z}_m | I_k} \mathbb{E}_{I_N | \pi_w, I_k, d_k, \dot{m}, \dot{\theta}_m, \dot{\eta}_m} \left[ \right. \\
&\quad \alpha_M \ln \frac{P(\dot{m} | I_N)}{q(\dot{m} | I_N; \phi_M)} + \alpha_\Theta \ln \frac{p(\dot{\theta}_m | I_N)}{q(\dot{\theta}_m | I_N; \phi_{\Theta_m})} + \alpha_Z \ln \frac{p(\dot{z}_m | I_N)}{q(\dot{z}_m | I_N; \phi_{Z_m})} \\
&\quad \left. - \alpha_M \ln \frac{P(\dot{m} | I_k)}{q(\dot{m} | I_k; \phi_M)} - \alpha_\Theta \ln \frac{p(\dot{\theta}_m | I_k)}{q(\dot{\theta}_m | I_k; \phi_{\Theta_m})} - \alpha_Z \ln \frac{p(\dot{z}_m | I_k)}{q(\dot{z}_m | I_k; \phi_{Z_m})} \right] \\
&= \mathbb{E}_{I_N | \pi_w, I_k, d_k} \left[ \alpha_M D_{\text{KL}}(P(m | I_N) || q(m | I_N; \phi_M)) \right. \\
&\quad \left. + \mathbb{E}_{m | I_N} [\alpha_\Theta D_{\text{KL}}(p(\theta_m | I_N) || q(\theta_m | I_N; \phi_{\Theta_m})) + \alpha_Z D_{\text{KL}}(p(z_m | I_N) || q(z_m | I_N; \phi_{Z_m}))] \right] \\
&\quad - \alpha_M D_{\text{KL}}(P(m | I_k) || q(m | I_k; \phi_M)) \\
&\quad - \mathbb{E}_{m | I_k} [\alpha_\Theta D_{\text{KL}}(p(\theta_m | I_k) || q(\theta_m | I_k; \phi_{\Theta_m})) + \alpha_Z D_{\text{KL}}(p(z_m | I_k) || q(z_m | I_k; \phi_{Z_m}))].
\end{aligned}$$

Applying the triangle inequality, the difference is bounded by

$$\begin{aligned}
& \left| Q_{I,k}^{\pi_w}(I_k, d_k) - Q_{I,k}^{\pi_w}(I_k, d_k; \phi) \right| \\
&\leq \mathbb{E}_{I_N | \pi_w, I_k, d_k} \left[ \alpha_M D_{\text{KL}}(P(m | I_N) || q(m | I_N; \phi_M)) \right. \\
&\quad \left. + \mathbb{E}_{m | I_N} [\alpha_\Theta D_{\text{KL}}(p(\theta_m | I_N) || q(\theta_m | I_N; \phi_{\Theta_m})) + \alpha_Z D_{\text{KL}}(p(z_m | I_N) || q(z_m | I_N; \phi_{Z_m}))] \right] \\
&\quad + \alpha_M D_{\text{KL}}(P(m | I_k) || q(m | I_k; \phi_M)) \\
&\quad + \mathbb{E}_{m | I_k} [\alpha_\Theta D_{\text{KL}}(p(\theta_m | I_k) || q(\theta_m | I_k; \phi_{\Theta_m})) + \alpha_Z D_{\text{KL}}(p(z_m | I_k) || q(z_m | I_k; \phi_{Z_m}))].
\end{aligned}$$

Therefore, the bias of the critic is contributed from both the bias of the final variational posterior  $q(\cdot | I_N; \phi_{(\cdot)})$  and the bias of the intermediate variational posteriors  $q(\cdot | I_k; \phi_{(\cdot)})$  for  $k = 1, \dots, N-1$ . It equals to zero if and only if all the variational posteriors are equal to their corresponding true posteriors (except the trivial case when  $\alpha_M = \alpha_\Theta = \alpha_Z = 0$ ).

The critic network (parameterized by  $\nu$ ) is updated after the update of the variational posterior approximation and the update of the *one-point IG*  $\dot{g}_k(I_k, d_k, y_k; \phi)$  and  $\dot{g}_N(I_N; \phi)$  during each outer iteration in Algorithm 1. It can be learned in a supervised learning manner by minimizing the loss function:

$$\mathcal{L}(\nu) = \frac{1}{n_{\text{batch}}} \sum_{i=1}^{n_{\text{batch}}} \sum_{k=0}^{N-1} \left[ Q_{k,\nu}^{\pi_w}(I_k^{(i)}, d_k^{(i)}) - \left( \dot{g}_k(I_k^{(i)}, d_k^{(i)}, y_k^{(i)}) + \gamma Q_{k+1,\nu}^{\pi_w}(I_{k+1}^{(i)}, d_{k+1}^{(i)}) \right) \right]^2,$$

where  $\gamma \in [0, 1]$  is a discount factor used for regularization, and batch samples are drawn from the replay buffer. When the TIG formulation is used, all the stage rewards  $\dot{g}_k$  for  $k = 0, \dots, N-1$  are 0 if there are no non-IG immediate rewards. In that case, the training of the critic network at early stages will be slow and may even lead to numerical divergence of the policy gradient when horizon  $N$  is long. Therefore, we utilize the idea of REINFORCE [53] and modify the loss function for TIG to

$$\begin{aligned}
\mathcal{L}(\nu) = \frac{1}{n_{\text{batch}}} \sum_{i=1}^{n_{\text{batch}}} \sum_{k=0}^{N-1} \left[ \right. & Q_{k,\nu}^{\pi_w}(I_k^{(i)}, d_k^{(i)}) \\
& - \psi \left( \dot{g}_k(I_k^{(i)}, d_k^{(i)}, y_k^{(i)}) + \gamma Q_{k+1,\nu}^{\pi_w}(I_{k+1}^{(i)}, d_{k+1}^{(i)}) \right) \\
& \left. - (1 - \psi) \left( \sum_{t=k}^{N-1} \gamma^{t-k} \dot{g}_t(I_t^{(i)}, d_t^{(i)}, y_t^{(i)}) + \gamma^{N-k} \dot{g}_N(I_N^{(i)}) \right) \right]^2,
\end{aligned}$$

where  $\psi$  linearly increases from 0 to 1 during the training process. Moreover, the target network in [36] is also utilized to enable off-policy learning with the update rate of the target network set to 0.1 across all numerical cases. The optimization of the critic network is carried out using Adam for all numerical cases.

### B.4.3 Numerical estimation of the policy gradient

The actor network is updated last during each outer iteration in Algorithm 1. The MC estimator of the policy gradient (Eqn. (18)) is

$$\nabla_w \dot{U}(w; \phi) \approx \frac{1}{n_{\text{batch}}} \sum_{i=1}^{n_{\text{batch}}} \sum_{k=0}^{N-1} \nabla_w \mu_{k,w}(I_k^{(i)}) \nabla_{d_k^{(i)}} Q_{k,\nu}^{\pi_w}(I_k^{(i)}, d_k^{(i)}) \Big|_{d_k^{(i)} = \mu_{k,w}(I_k^{(i)})}.$$

In our implementation, we draw batch samples from a replay buffer. The optimization of the actor network is performed with Adam for all numerical cases.

### B.4.4 Exploration versus exploitation

To promote better exploration during the optimization process, an exploration policy is constructed by adding perturbation to the deterministic policy:

$$d_k = \mu_k(I_k) + \epsilon_{\text{explore}},$$

where  $\epsilon_{\text{explore}}$  follows a zero-mean multivariate Gaussian distribution with a diagonal covariance. The covariance diagonal terms reflect the exploration length scale for each dimension of  $d_k$ . If perturbing to outside the feasible design region  $\mathcal{D}_k$ , it will be moved back to the closest feasible point. A good balance of exploration and exploitation is important for the numerical algorithm to find a good policy. Insufficient exploration limits the understanding of the environment, while too much exploration (i.e. insufficient exploitation) may lead to slow convergence. A reasonable strategy is to set a larger exploration in the early stages of training and then gradually reduce it. Details of these exploration settings will be specified for each numerical case in Appendix C.

We emphasize that the policy exploration is employed solely during the training phase. During evaluation (testing), the deterministic policy is still utilized without additional exploration.

### B.4.5 Hyperparameter tuning

Since vsOED is trained with limited budgets in this work, our main strategy for hyperparameter tuning is to start with a relatively large hyperparameter value and gradually decrease it.

For the optimization of the model posterior predictor and the parameter posterior predictor with GMM and NFs, we start with the initial learning rate  $10^{-3}$  and an exponential learning rate decay rate 0.9999.

For the optimization of the critic network, an initial learning rate of  $10^{-3}$  and a learning rate decay rate of 0.9999 are used across all numerical cases. Both the variational approximation and the critic network are updated 5 steps (i.e. applying gradient ascent steps 5 times) within each outer iteration. It is important to note that updating the variational approximation and the critic network too many steps in each outer iteration may result in overestimation of the value function and adversely affect the policy search [26].

For the optimization of the actor network, a learning rate decay rate of 0.9999 is used. However, the choice of the initial learning rate is more problem-dependent. Typically, we start with an initial learning rate of  $10^{-3}$  and gradually decrease it to  $5 \times 10^{-4}$  or  $2 \times 10^{-4}$  if divergence occurs. For IIG formulation, an initial learning rate of  $10^{-3}$  works well. However, for TIG formulation, a smaller actor learning rate is required. This is because the learning of the critic in TIG is slower, and a large actor learning rate can more easily induce divergence in the early stages of training.

For other hyperparameters, including the number of updates  $n_{\text{update}}$ , the number of new MC episodes  $n_{\text{episode}}$ , the batch size  $n_{\text{batch}}$ , the replay buffer size  $n_{\text{buffer}}$ , a number of combinations are tested to select the optimal combination and their values are specified for each numerical case in Appendix C.

## B.5 Baselines

The key properties of methods compared in this study are summarized in Table 10.

Table 10: Properties of different methods.

	Real-time	Adaptive	Implicit	No model derivative	Multi-model
Random	✓	✗	✓	✓	✓
DAD	✓	✓	✗	✗	✗
iDAD	✓	✓	✓	✗	✗
RL	✓	✓	✗	✓	✗
vsOED	✓	✓	✓	✓	✓

### B.5.1 Random

For Random design, a design is sampled uniformly within  $\mathcal{D}$ .

### B.5.2 DAD

For DAD [19], we use the code available at <https://github.com/ae-foster/dad>. The default setup is used as the full training, while for limited budgets, different combinations of hyperparameters are tested to select the optimal one.

### B.5.3 iDAD

For iDAD [30], we use the code available at <https://github.com/desi-ivanova/idad>. The default setup is used as the full training but the learning rate is set as 0.0002, while for limited budgets, different combinations of hyperparameters are tested to select the optimal one.

### B.5.4 RL

For RL [5], we use the code available at <https://github.com/csiro-mlai/RL-BOED>. The default setup is used as the full training, while for limited budgets, different combinations of hyperparameters are tested to select the optimal one.

## C Experiment details

### C.1 Software details

All experiments are implemented in Python using PyTorch. Truncated normal distribution is not naturally supported by PyTorch, we use the code from [https://github.com/toshas/torch\\_truncnorm](https://github.com/toshas/torch_truncnorm). The solver of the SIR model is from <https://github.com/desi-ivanova/idad>.

### C.2 Hardware details

All experiments are run on the Great Lakes Slurm HPC Cluster nodes <https://arc.umich.edu/greatlakes/configuration/>, each node is equipped with a single Nvidia Tesla A40 or V100 GPU.

### C.3 Prior contrastive estimation

When nuisance parameters  $\eta$  are not present, the reward corresponding to PoIs under the *one-point estimate* formulation can also be estimated by

$$\begin{aligned}
& \ln \frac{p(\dot{\theta}_m | I_{k_2})}{p(\dot{\theta}_m | I_{k_1})} \\
&= \ln \frac{p(I_{k_2} | \dot{m}, \dot{\theta}_m) p(I_{k_1})}{p(I_{k_1} | \dot{m}, \dot{\theta}_m) p(I_{k_2})} \\
&\approx \ln \frac{p(I_{k_2} | \dot{m}, \dot{\theta}_m)^{\frac{1}{L+1}} \left[ p(I_{k_1} | \dot{m}, \dot{\theta}_m) + \sum_{l=1}^{L_m} p(I_{k_1} | \dot{m}, \theta_{m,l}) \right]}{p(I_{k_1} | \dot{m}, \dot{\theta}_m)^{\frac{1}{L+1}} \left[ p(I_{k_2} | \dot{m}, \dot{\theta}_m) + \sum_{l=1}^{L_m} p(I_{k_2} | \dot{m}, \theta_{m,l}) \right]},
\end{aligned}$$

where the first equality follows Bayes' rule,  $\theta_{m,l} \sim p(\theta_m)$  are  $L_m$  contrastive i.i.d. samples, which are shared in the numerator and denominator in the last equation, and  $0 \leq k_1 < k_2 \leq N$ . When  $k_1 = 0$  and  $k_2 = N$ , it is the estimate for the terminal *one-point-IG*, and when  $k_1 = k$  and  $k_2 = k+1$ , it is the estimate for the incremental *one-point-IG* at the  $k$ th stage. PCE forms a lower bound of the EIG, and the bound becomes tight as  $L_m \rightarrow \infty$  [19]. Note that PCE cannot be practically applied when  $\eta$  is present, since evaluating the likelihood  $p(I_k|\dot{m}, \theta_{m,l})$  would require yet another loop to marginalize out  $\eta_m$  and is extremely expensive. Similarly, PCE also cannot be practically applied for estimating the reward of IG on the goal-oriented predictive QoIs, which requires another loop to marginalize out  $\theta_m$  and  $\eta_m$ .

The reward of IG on model probability using the *one-point estimate* can also be rewritten as

$$\begin{aligned} & \ln \frac{P(\dot{m}|I_{k_2})}{P(\dot{m}|I_{k_1})} \\ &= \ln \frac{p(I_{k_2}|\dot{m})p(I_{k_1})}{p(I_{k_1}|\dot{m})p(I_{k_2})} \\ &= \ln \frac{p(I_{k_2}|\dot{m}) \sum_{m=1}^M P(m)p(I_{k_1}|m)}{p(I_{k_1}|\dot{m}) \sum_{m=1}^M P(m)p(I_{k_2}|m)}, \end{aligned}$$

where each marginalized likelihood  $p(I_k|m)$  may be estimated by

$$\begin{aligned} p(I_k|m) &= \int_{\Theta, H} p(\theta_m, \eta_m|m)p(I_k|m, \theta_m, \eta_m) d\theta_m d\eta_m \\ &\approx \frac{1}{L_m} \sum_{l=1}^{L_m} p(I_k|m, \theta_{m,l}, \eta_{m,l}), \end{aligned}$$

with  $\theta_{m,l}$  and  $\eta_{m,l}$  being samples independently drawn from the joint prior  $p(\theta_m, \eta_m|m)$ . To ensure an accurate estimate during the evaluation stage to compare the policies found by different methods, we use a large sample size  $L_m \approx \frac{10^6}{M}$ .

#### C.4 Source location finding

In this numerical case, we enlist  $M = 3$  candidate models with uniform model prior (i.e.  $P(m) = 1/3$ ). For the  $m$ th model ( $m \in \{1, 2, 3\}$ ), there are  $m$  sources randomly located in a 2D domain, each emitting a signal that decays inversely with the square of the distance. The PoIs are the source locations  $\theta_m = \{\theta_{m,1}, \dots, \theta_{m,m}\}$  where  $\theta_{m,i} \in \mathbb{R}^2$  denotes the location of  $i$ th source. The total intensity at a given location  $d$ , aggregated from the  $m$  sources, is then

$$\mu(m, \theta_m, d) = \epsilon_{bg} + \sum_{i=1}^m \frac{1}{\epsilon_{max} + \|\theta_{m,i} - d\|^2},$$

where  $\epsilon_{bg} = 10^{-1}$  is the background signal, and  $\epsilon_{max} = 10^{-4}$  is the maximum signal. The likelihood follows

$$\log y|m, \theta_m, d \sim \mathcal{N}(\log \mu(m, \theta_m, d), \sigma^2),$$

where the noise standard deviation is  $\sigma = 0.5$ . The prior is

$$\theta_{m,i} \sim \mathcal{N}(0, I).$$

The design space is restricted to  $\mathcal{D}_k = [-4, 4]^2$ .

We are also interested in a goal-oriented OED situation that involves the flux along the  $x$  spatial direction, which can be computed using Fick's law:

$$f(m, \theta_m, d) = -D \frac{\partial \mu(m, \theta_m, d)}{\partial x},$$

where  $f$  represents the flux, and  $D = 1$  is the diffusivity. More specifically, we consider the flux integrated over an infinite vertical wall located at  $x = 6$ , which yields

$$\begin{aligned} J(m, \theta_m) &= \int_{y=-\infty}^{+\infty} f(m, \theta_m, (6, y)) dy \\ &= \sum_{i=1}^m - \frac{\pi(\theta_{m,i,x} - 6)}{(\epsilon_{max} + (\theta_{m,i,x} - 6)^2)^{3/2}}. \end{aligned}$$

The final goal-oriented QoI is the log flux magnitude  $z_m = \log |J(m, \theta_m)|$ . It is worth noting that the flux is only depending on the  $x$ -position of the source (i.e.  $\theta_{m,i,x}$ ). Since the explicit form of the prior-predictive for the QoI is not analytically available, we elect to omit it from the computations and it does not affect the optimal policy per Appendix A.5.

#### C.4.1 Uni-model example

In the uni-model example,  $m$  is fixed at 2.

**Hyperparameters.** The hyperparameters for the uni-model source location finding problem are listed in Table 11, where vsOED-G-I stands for GMM with IIG, and vsOED-N-T for NF with TIG, etc. For the linear mapping in the output layer of the GMM net, we transform the output of the GMM mean net of the PoI posterior predictor to a range of  $[-6, 6]$ , the output of the GMM standard deviation net of the PoI posterior predictor to a range of  $[10^{-5}, 1]$ , the output of the GMM mean net of the QoI posterior predictor to a range of  $[-6, 6]$ , and the output of the GMM standard deviation net of the QoI posterior predictor to a range of  $[10^{-5}, 2]$ . The truncated normal distribution is not used in this example.

Table 11: Hyperparameters of the uni-model source location finding problem. In the table, “lr” means “learning rate”.

	vsOED-G-T	vsOED-G-I	vsOED-F-T	vsOED-F-I
#training iteration $n_{\text{update}}$	10001	10001	10001	10001
#new episodes per iteration $n_{\text{episode}}$	1000	1000	1000	1000
batch size $n_{\text{batch}}$	10000	10000	10000	10000
parameter predictor initial lr	$10^{-3}$	$10^{-3}$	$10^{-3}$	$10^{-3}$
parameter predictor lr decay	0.9999	0.9999	0.9999	0.9999
#param predictor update per iteration	5	5	5	5
$n_{\text{mixture}}$	8	8	N/A	N/A
$n_{\text{trans}}$	N/A	N/A	4	4
initial actor lr	$5 \times 10^{-4}$	$10^{-3}$	$10^{-3}$	$10^{-3}$
actor lr decay	0.9999	0.9999	0.9999	0.9999
initial critic lr	$10^{-3}$	$10^{-3}$	$10^{-3}$	$10^{-3}$
critic lr decay	0.9999	0.9999	0.9999	0.9999
max buffer size	$10^6$	$10^6$	$10^6$	$10^6$
discount factor $\gamma$	1	0.9	1	0.9
initial design noise scale	0.5	0.5	0.5	0.5
design noise scale decay	0.9999	0.9999	0.9999	0.9999
target network lr	0.1	0.1	0.1	0.1

**Training stability.** Figure 8 shows the training histories of the PoI inference OED ( $\alpha_\Theta = 1$ ) and the QoI goal-oriented OED ( $\alpha_Z = 1$ ), where the solid line and the shaded region are the mean and standard error of 4 replicates with different random seeds. The training of vsOED appears highly robust against randomization. Table 12 presents the PCE evaluation of optimal policies from 4 replicates of PoI inference OED, optimized for horizon  $N = 30$ . Each element in the table represents the mean and standard error computed from 2000 samples. Table 13 further provides the mean and standard error aggregated from the means of these 4 replicates. These tables further demonstrate the robustness of vsOED. Moreover, we observe that vsOED with NF achieves slightly better performance compared to using GMM. This can be attributed to the increased expressiveness of NFs. Figure 9 provides insights into the expressiveness of NFs, from which we can find that when the posterior is highly non-Gaussian, NF outperforms GMM in approximating the posterior. However, as the horizon  $N$  increases, the posterior tends toward sharper multi-modal Gaussian mixtures, which explains the similar performance of using GMM and NFs at horizon  $N = 30$ . Figure 10 draws the variational expected utility lower bounds against the number of experiments for the goal-oriented OED. It also demonstrates the robustness of vsOED.

**Calculation of the goal-oriented posterior.** The true posterior-predictive PDF of the goal-oriented QoI  $z$  shown in Fig. 4 are calculated on a discretized grid, where the prior  $p(z)$  is obtained using kernel density estimation (KDE) [49] with  $10^6$  prior  $z$  samples, and the likelihood  $p(I_N|z, \pi)$  is

obtained with approximate Bayesian computation (ABC) [12]:

$$p(I_N|z, \pi) \approx \frac{1}{n_{\text{accept}}} \sum_{i=1}^L p(I_N|\theta^{(i)}, \pi) \mathbf{1}_{|H(\theta^{(i)})-z| \leq \epsilon},$$

where  $\theta^{(i)} \sim p(\theta)$ ,  $\mathbf{1}$  is an indicator function and  $n_{\text{accept}}$  is the number of  $\theta$  samples that satisfy the indicator function. We use  $L = 10^6$  samples and acceptance tolerance  $\epsilon = 10^{-3}$  to ensure accuracy.

More results about the uni-model source location finding can be found in Sec. 6.1 in the main paper.

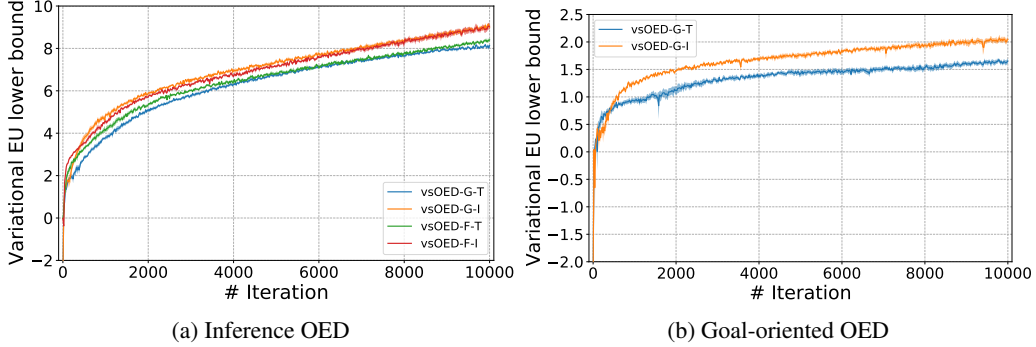


Figure 8: Training histories of PoI inference OED and QoI goal-oriented OED for the uni-model source location finding problem, optimized for horizon  $N = 30$ . The solid line and the shaded region are the mean and standard error of 4 replicates with different random seeds.

Table 12: PCE evaluation of optimal policies from 4 replicates of PoI inference OED for the uni-model source location finding problem, optimized for horizon  $N = 30$ .

	Run 1	Run 2	Run 3	Run 4
vsOED-G-T	11.257 ± 0.046	11.089 ± 0.046	11.237 ± 0.046	11.022 ± 0.044
vsOED-G-I	12.496 ± 0.040	12.306 ± 0.043	12.577 ± 0.040	11.895 ± 0.044
vsOED-F-T	11.239 ± 0.046	11.674 ± 0.045	11.149 ± 0.046	11.592 ± 0.045
vsOED-F-I	12.393 ± 0.042	12.342 ± 0.042	12.155 ± 0.042	12.536 ± 0.043

Table 13: Aggregated PCE evaluation results of optimal policies from 4 replicates of PoI inference OED for the uni-model source location finding problem, optimized for horizon  $N = 30$ .

	Mean	SE
vsOED-G-T	11.151	0.049
vsOED-G-I	12.319	0.132
vsOED-F-T	11.414	0.112
vsOED-F-I	12.357	0.068

### C.4.2 Multi-model example

For the multi-model source location finding problem, 5 scenarios will be considered: model discrimination OED ( $\alpha_M = 1, \alpha_\Theta = \alpha_Z = 0$ ), inference OED ( $\alpha_\Theta = 1, \alpha_M = \alpha_Z = 0$ ), goal-oriented OED ( $\alpha_Z = 1, \alpha_M = \alpha_\Theta = 0$ ), discrimination-inference OED ( $\alpha_M = \alpha_\Theta = 1, \alpha_Z = 0$ ) and discrimination-goal-oriented OED ( $\alpha_M = \alpha_Z = 1, \alpha_\Theta = 0$ ).

**Hyperparameters.** The hyperparameters are listed in Table 14. The linear mapping in the output layer of the GMM net is the same as the uni-model example in Appendix C.4.1.

**Training stability.** For the multi-model source location finding, the investigation of training stability is illustrated here only on the inference OED scenario. Figure 11 shows the training histories of

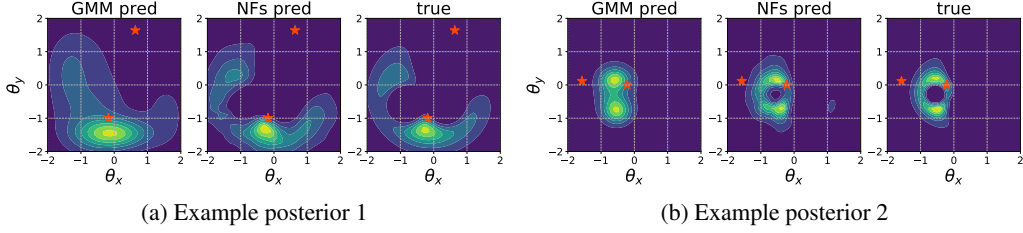


Figure 9: Examples of GMM posterior, NF posterior, and true posterior at horizon  $N = 3$ . Red stars are the true source locations.

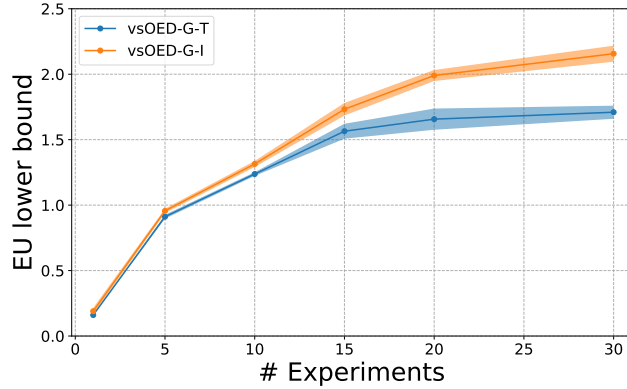


Figure 10: Variational expected utility lower bounds of goal-oriented OED for the uni-model source location finding problem. The solid line and the shaded region are the mean and standard error of 4 replicates with different random seeds.

Table 14: Hyperparameters of the multi-model source location finding problem.

	vsOED-G-T	vsOED-G-I
#training iteration $n_{\text{update}}$	10001	10001
#new episodes per iteration $n_{\text{episode}}$	1000	1000
batch size $n_{\text{batch}}$	10000	10000
model predictor initial lr	$10^{-3}$	$10^{-3}$
model predictor lr decay	0.9999	0.9999
#model predictor update per iteration	5	5
parameter predictor initial lr	$10^{-3}$	$10^{-3}$
parameter predictor lr decay	0.9999	0.9999
#param predictor update per iteration	5	5
$n_{\text{mixture}}$	8	8
initial actor lr	$2 \times 10^{-4}$	$10^{-3}$
actor lr decay	0.9999	0.9999
initial critic lr	$10^{-3}$	$10^{-3}$
critic lr decay	0.9999	0.9999
max buffer size	$10^6$	$10^6$
discount factor $\gamma$	1	0.9
initial design noise scale	0.5	0.5
design noise scale decay	0.9999	0.9999
target network lr	0.1	0.1

the inference OED, where the solid line and the shaded region are the mean and standard error of 4 replicates with different random seeds. Similar to the uni-model case, the training of vsOED appears highly robust against randomization. Table 15 presents the PCE evaluation of optimal policies from 4 replicates of inference OED, optimized for horizon  $N = 30$ . Each element in the table represents the mean and standard error computed from 2000 samples. Table 16 further provides the mean and standard error aggregated from the means of these 4 replicates. These results further support that vsOED is robust under different random seeds.

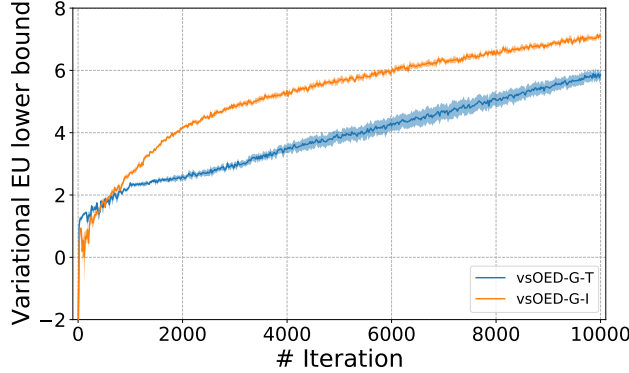


Figure 11: Training histories of PoI inference OED for the multi-model source location finding problem, optimized for horizon  $N = 30$ . The solid line and the shaded region are the mean and standard error of 4 replicates with different random seeds.

Table 15: PCE evaluation of optimal policies from 4 replicates of inference OED for the multi-model source location finding problem, optimized for horizon  $N = 30$ .

	Run 1	Run 2	Run 3	Run 4
vsOED-G-T	$9.672 \pm 0.055$	$9.263 \pm 0.055$	$9.058 \pm 0.057$	$8.833 \pm 0.056$
vsOED-G-I	$10.567 \pm 0.048$	$10.085 \pm 0.049$	$10.464 \pm 0.050$	$10.429 \pm 0.048$

Table 16: Aggregated PCE evaluation results of optimal policies from 4 replicates of inference OED for the multi-model source location finding problem, optimized for horizon  $N = 30$ .

	Mean	SE
vsOED-G-T	9.206	0.154
vsOED-G-I	10.386	0.090

**Expected utilities.** Figure 12 plots the expected utilities of various OED scenarios, averaged over 2 replicates. The IIG formulation demonstrates greater stability and higher performance, especially when the horizon  $N$  is longer than 15.

**Policies.** Figure 13 plots example designs for various OED scenarios. The model discrimination OED tends to do more exploration, while the inference OED tends to exploit the knowledge about the source location. Similar to the uni-model example, the goal-oriented OED prefers to take vertical measurements. The discrimination-inference OED and the discrimination-goal-oriented OED appear slightly more exploratory than the inference OED and the goal-oriented OED, respectively.

**Model discrimination.** Figure 14 illustrates the true model posteriors and the posteriors predicted by the model posterior predictor of the model discrimination OED, optimized for horizon  $N = 30$ . The policy learned by the model discrimination OED is effective in distinguishing between different models, and the predicted distributions from the model posterior predictor align well with the true posteriors.

To further illustrate that the model discrimination OED has found a good policy, we compare the EIG on model probability of various OED scenarios optimized for horizon  $N = 30$  in Table 17. The EIG

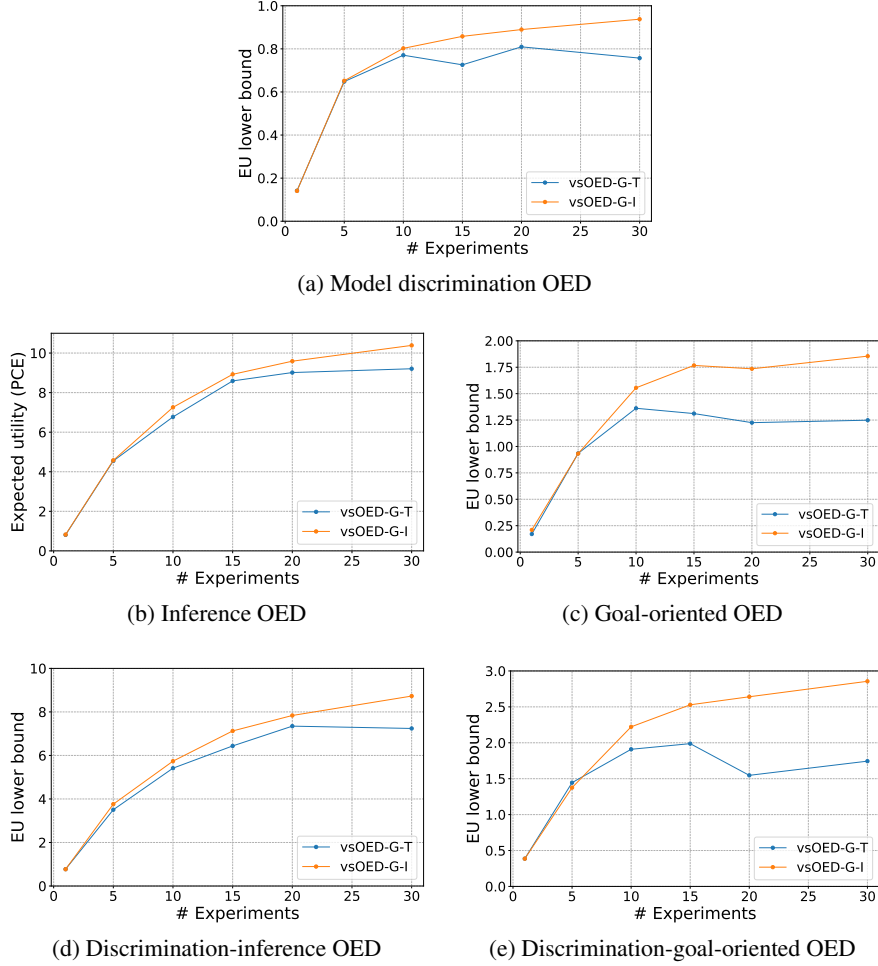


Figure 12: Expected utilities of various OED scenarios for the multi-model source location finding problem, averaged over 2 replicates. Variational lower bounds with  $10^6$  samples are presented except for inference OED, where PCE with 2000 samples and  $L = 10^6$  is used for evaluation.

is calculated by PCE with 2000 samples and  $L_m \approx \frac{10^6}{3}$  for  $m = 1, 2, 3$ . The model discrimination OED finds the optimal policy in terms of maximizing the EIG on model probability. The EIG on the model probability in the discrimination-inference OED and discrimination-goal-oriented OED are also higher than that of inference OED and goal-oriented OED, respectively.

Table 17: EIG on model probability for various OED scenarios optimized for horizon  $N = 30$ .

	Mean	SE
model discrimination OED	1.020	0.003
inference OED	0.896	0.005
goal-oriented OED	0.815	0.005
discrimination-inference OED	0.950	0.005
discrimination-goal-oriented OED	0.967	0.004

**PoI inference.** Table 18 lists the EIG on the PoI for various OED scenarios optimized for horizon  $N = 30$ . The EIG is calculated by PCE with 2000 samples and  $L_m \approx \frac{10^6}{3}$  for  $m = 1, 2, 3$ . As expected, the inference OED finds the best policy in terms of maximizing the EIG on PoI inference.

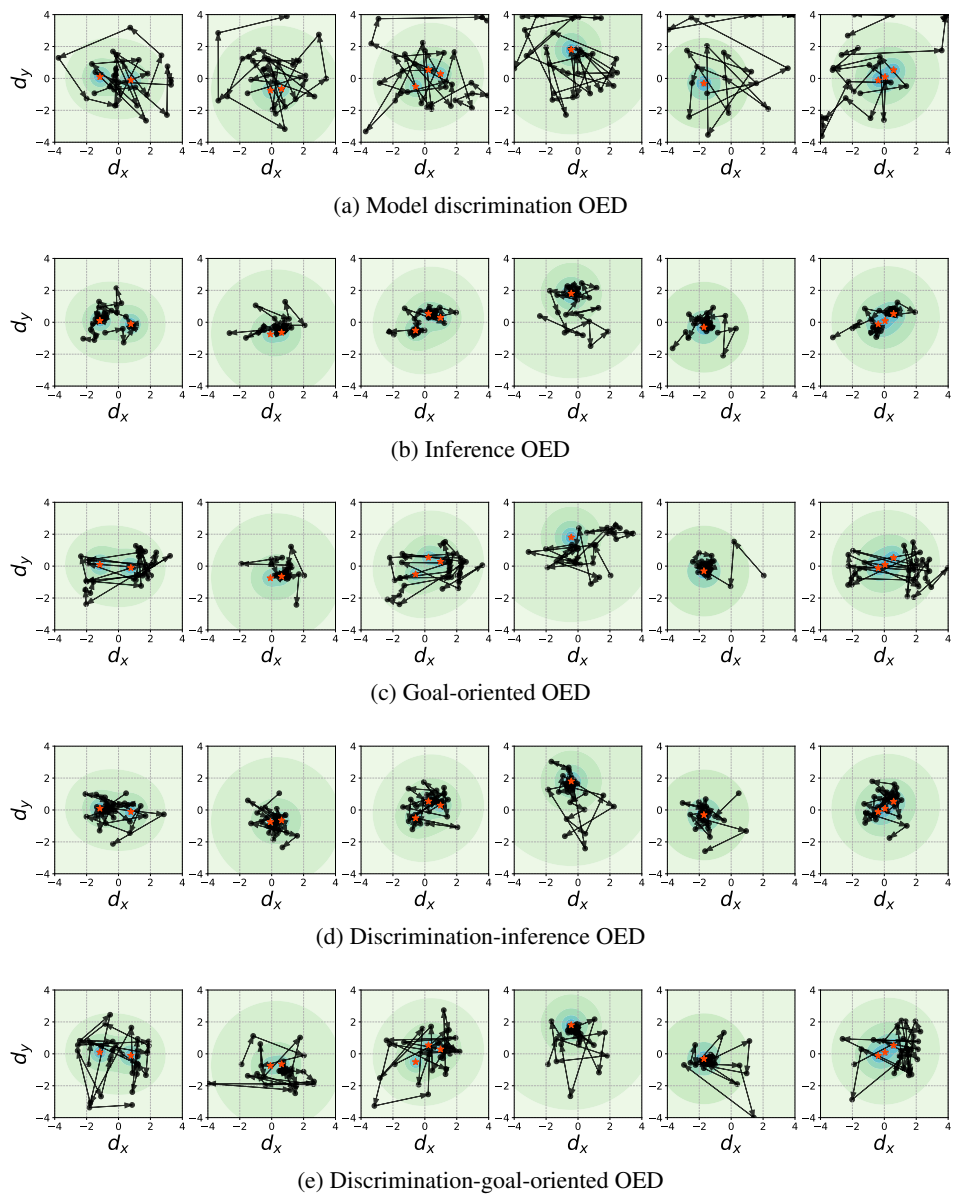


Figure 13: Example designs of various OED scenarios for the multi-model source location finding problem, optimized for horizon  $N = 30$ .

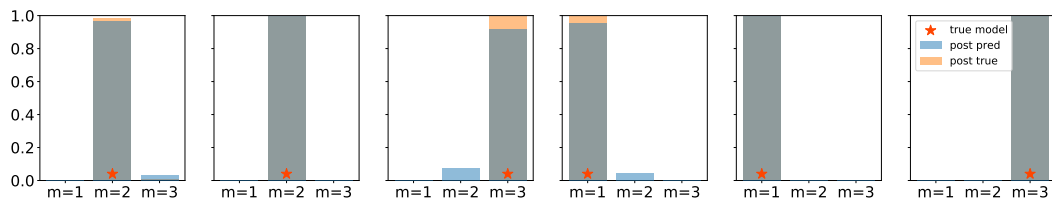


Figure 14: Example model posteriors from the model discrimination OED optimized for horizon  $N = 30$ .

Table 18: EIG on the PoI for various OED scenarios optimized for horizon  $N = 30$ .

	Mean	SE
model discrimination OED	5.956	0.065
inference OED	10.567	0.048
goal-oriented OED	6.999	0.053
discrimination-inference OED	10.330	0.049
discrimination-goal-oriented OED	7.830	0.052

### C.5 Constant Elasticity of Substitution

This experiment involves a single model, and was previously studied in [20, 21, 5]. Constant Elasticity of Substitution (CES) falls under the domain of behavioral economics, where participants are presented with two baskets  $x$  and  $x'$  of goods and asked to assess the subjective difference in utility between the two baskets. The participants rate this difference on a sliding scale ranging from 0 to 1. The CES model [2] is then used to model the underlying utility function with latent PIs  $\theta = (\rho, \beta, \log u)$  with the following prior:

$$\begin{aligned} \rho &\sim \text{Beta}(1, 1) \\ \beta &\sim \text{Dirichlet}([1, 1, 1]) \\ \log u &\sim \mathcal{N}(1, 3^2). \end{aligned}$$

It is worth noting that the degree of freedom of  $\beta$  is 2 as the sum of  $\beta_i$  for  $i = 1, 2, 3$  is 1, therefore, only  $\beta_1$  and  $\beta_2$  are included in  $\theta$ . The design variable is  $d = (x, x')$  where  $x, x' \in [0, 100]^3$  represent the baskets of goods. The forward model is

$$\begin{aligned} U(x) &= \left( \sum_i x_i^\rho \beta_i \right)^{\frac{1}{\rho}} \\ \mu_\eta &= u \cdot (U(x) - U(x')) \\ \sigma_\eta &= \tau u \cdot (1 + \|x - x'\|) \\ \eta &\sim \mathcal{N}(\mu_\eta, \sigma_\eta^2) \\ y &= \text{clip}(\text{sigmoid}(\eta), \epsilon, 1 - \epsilon), \end{aligned} \tag{25}$$

where  $\tau = 0.005$  and  $\epsilon = 2^{-22}$ .

**Hyperparameters.** The hyperparameters are listed in Table 19. We only use vsOED with TIG formulation since the horizon of this problem is at most 10. For the linear mapping in the output layer of the GMM net, we transform the output of the GMM mean net of the PoI posterior predictor to a range of  $[-1, 2]$  for  $\rho$  and  $\beta$ ,  $[-17, 19]$  for  $\log u$ , and the output of the GMM standard deviation net of the PoI posterior predictor to a range of  $[10^{-5}, 3]$  for all variables. The truncated normal distribution is used on  $\rho$  and  $\beta$  with support  $[0, 1]$ .

**Training stability.** Figure 15 shows the training histories of the CES problem, where the solid line and the shaded region are the mean and standard error of 4 replicates with different random seeds. The training process of the CES problem exhibits slightly more noise compared to the source location finding problem, but overall remains robust against randomization. Table 20 presents the PCE evaluation results of 4 replicates optimized for horizon  $N = 10$ . Each element in the table represents the mean and standard error computed from 2000 samples. Table 21 further provides the mean and standard error aggregated from the means of these 4 replicates.

**Expected utilities.** Figure 16a presents the expected cumulative utilities at various experiment stages, where all policies are optimized for a design horizon of  $N = 10$  experiments and then evaluated on the various intermediate experiment stages. We restrict vsOED training to a total budget of 10 million episode samples, while fully training RL, DAD and iDAD using (RL 8 trillion episodes, DAD 100 billion episodes, and iDAD 200 million episodes). In Fig. 16b, we draw the expected utility plotted against the design horizon  $N$ . Each data point represents a new policy optimized for a specific design horizon. The computational budget of 10 million episodes is equally allocated to all methods for a fair comparison. Figure 16a demonstrates that the performance of vsOED with GMM

Table 19: Hyperparameters for the CES problem.

	vsOED-G-T	vsOED-F-T
#training iteration $n_{\text{update}}$	10001	10001
#new episodes per iteration $n_{\text{episode}}$	1000	1000
batch size $n_{\text{batch}}$	10000	10000
parameter predictor initial lr	$10^{-3}$	$10^{-3}$
parameter predictor lr decay	0.9999	0.9999
#param predictor update per iteration	5	5
$n_{\text{mixture}}$	8	N/A
$n_{\text{trans}}$	N/A	4
initial actor lr	$10^{-3}$	$10^{-3}$
actor lr decay	0.9999	0.9999
initial critic lr	$10^{-3}$	$10^{-3}$
critic lr decay	0.9999	0.9999
max buffer size	$10^6$	$10^6$
discount factor $\gamma$	1	1
initial design noise scale	5	5
design noise scale decay	0.9998	0.9998
target network lr	0.1	0.1

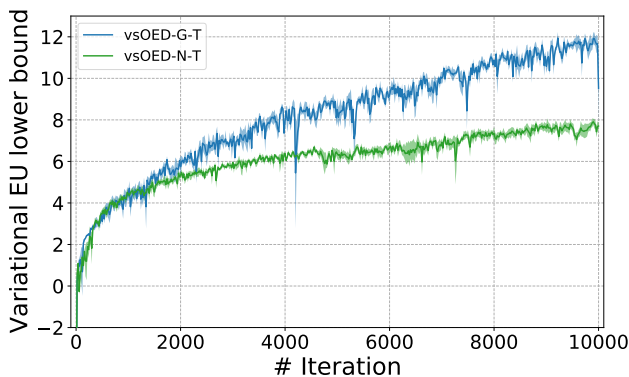


Figure 15: Training histories for the CES problem, optimized for horizon  $N = 10$ . The solid line and the shaded region are the mean and standard error of 4 replicates with different random seeds.

Table 20: PCE evaluation of optimal policies from 4 replicates of PoI inference OED for the CES problem, optimized for horizon  $N = 10$ .

	Run 1	Run 2	Run 3	Run 4
vsOED-G-T	$11.785 \pm 0.068$	$12.340 \pm 0.059$	$12.290 \pm 0.058$	$11.125 \pm 0.079$
vsOED-F-T	$8.401 \pm 0.098$	$9.510 \pm 0.086$	$8.908 \pm 0.087$	$10.299 \pm 0.081$

Table 21: Aggregated PCE evaluation of optimal policies from 4 replicates of PoI inference OED for the CES problem, optimized for horizon  $N = 10$ .

	Mean	SE
vsOED-G-T	11.885	0.245
vsOED-F-T	9.280	0.354

and TIG is slightly inferior to the fully-trained RL but significantly better than fully-trained DAD and iDAD. The lower values for vsOED with GMM and TIG in the earlier stages indicate that the policy prioritizes long-term expected utility over short-term rewards. In Fig. 16b, it is evident that under a common budget, vsOED with GMM and TIG outperforms other baseline methods for all values of  $N$ . Furthermore, the shaded regions in Fig. 16b represent the robustness of vsOED-G-T and RL training against random seeds. On the other hand, vsOED-F-T and DAD exhibit higher noise.

In this example, the performance of vsOED with NF is significantly worse compared to vsOED with GMM. This can be attributed to the limitation of NFs, as they are designed to handle random variables with infinite support, while in this case both  $\rho$  and  $\beta$  have finite support.

Figure 17 compares the posterior predicted by GMM and the true posterior. The GMM performs well in predicting  $\log u$ , but it tends to have wider posterior predictions for  $\rho$  and  $\beta$  compared to the true posterior. This is due to the nature of the CES problem, where many observations are clipped at the two ends as shown in Eqn. (25). Consequently, there are numerous observations with identical values, which makes it challenging for GMM to accurately learn the mapping from designs and observations to the posterior distribution. Nevertheless, despite the challenges in predicting the posterior accurately, vsOED with GMM is still able to find a good policy.

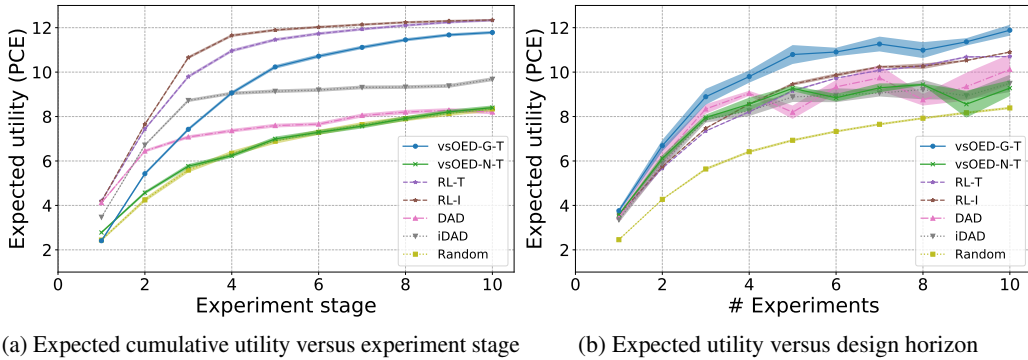


Figure 16: Expected utilities of various OED methods for the CES problem, all estimated using PCE with  $L = 10^6$ . (a) Mean and standard error (shaded) from 2000 evaluation episodes. (b) Mean and standard error (shaded) of 4 replicates with different random seeds, each replicate evaluated with 2000 episodes.

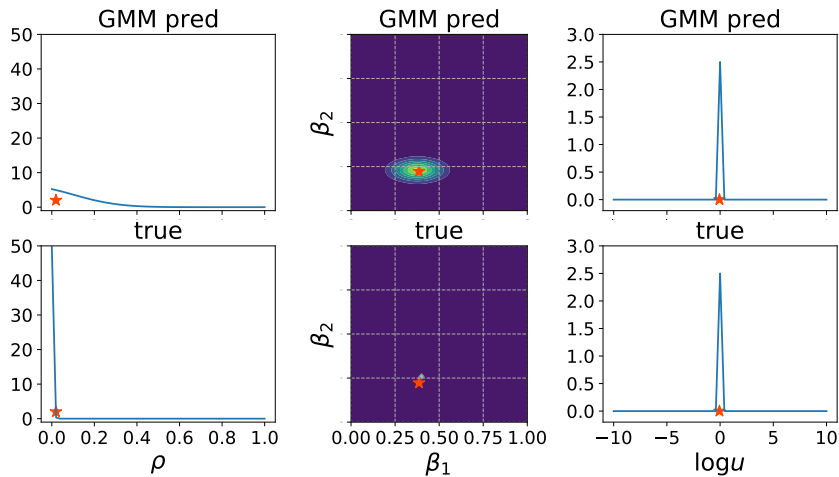


Figure 17: Examples of GMM posterior and true posterior for the CES problem at horizon  $N = 10$ . Red stars are the parameter values.

## C.6 SIR model

The experiment only involves a single model and was previously studied in [30]. The SIR model problem aims to estimate the infection rate  $\beta$  and the recovery rate  $\rho$ . Given a fixed population of size  $N$ , each individual starts from a susceptible state ( $S$ ) ( $\tau$  is time) to an infected state  $I(\tau)$  with rate  $\beta$ , and then recovers back to the recovered state  $R(\tau)$  with rate  $\rho$ .

The stochastic versions of SIR is usually defined by a continuous-time Markov chain (CTMC), which can be sampled via the Gillespie algorithm [1]. However, this generally yields discrete population states that have undefined gradients. We follow [30] to an alternative simulation algorithm that uses stochastic differential equations (SDEs), where yields continuous state populations and gradients can be approximated.

The population state vector is defined to be  $\mathbf{X}(\tau) = (S(\tau), I(\tau))^T$ , where  $R(\tau)$  can be ignored as the population size is fixed. The system of Itô SDEs that defines the stochastic SIR model is given by:

$$d\mathbf{X}(\tau) = \mathbf{f}(\mathbf{X}(\tau))d\tau + \mathbf{G}(\mathbf{X}(\tau))d\mathbf{W}(\tau) \quad (26)$$

where  $\mathbf{f}$  is the drift vector,  $\mathbf{G}$  is the diffusion matrix, and  $\mathbf{W}(\tau)$  is a vector of independent Wiener processes (also called Brownian motion). From [35], the drift vector and diffusion matrix are

$$\mathbf{f}(\mathbf{X}(\tau)) = \begin{pmatrix} -\beta \frac{S(\tau)I(\tau)}{N} \\ \beta \frac{S(\tau)I(\tau)}{N} - \rho I(\tau) \end{pmatrix} \quad \text{and} \quad \mathbf{G}(\mathbf{X}(\tau)) = \begin{pmatrix} -\sqrt{\beta \frac{S(\tau)I(\tau)}{N}} & 0 \\ \sqrt{\beta \frac{S(\tau)I(\tau)}{N}} & -\sqrt{\rho I(\tau)} \end{pmatrix}. \quad (27)$$

Given Eqn. (26) and (27), we can simulate state populations  $\mathbf{X}(\tau)$  by solving the SDE using finite-differencing methods, such as the Euler-Maruyama method. For a fair comparison, we follow [30] and just use the solutions of Eqn. (26) as data and do not consider an additional Poisson observational model that increases the noise in simulated data as suggested in [35].

The PoIs of this example are the logarithmic infection rate  $\log \beta$  and the logarithmic recovery rate  $\log \rho$  with the following prior:

$$\begin{aligned} \log \beta &\sim \mathcal{N}(\log 0.5, 0.5^2) \\ \log \rho &\sim \mathcal{N}(\log 0.1, 0.5^2). \end{aligned}$$

The design variable  $d$  is the time  $\tau \in [0, 100]$  for taking measurements, where the observable is the number of infected people  $I(\tau)$ .  $I(\tau)$  can be obtained by solving Eqn. (26). To accelerate the training process, we pre-generate and store 1 million simulations, and access the stored simulations during the training. A new set of  $3 \times 10^5$  simulations are used as evaluation data.

**Hyperparameters.** The hyperparameters are listed in Table 22. We only use vsOED with TIG formulation since the horizon of this problem is at most 10. For the linear mapping in the output layer of the GMM net, we transform the output of the GMM mean net of the PoI posterior predictor to a range of  $[-6, 4]$ , and the output of the GMM standard deviation net of the PoI posterior predictor to a range of  $[10^{-5}, 0.5]$  for all variables. The truncated normal distribution is not used in this case.

**Training stability.** Figure 18 presents the training histories for the CES problem, where the solid line and the shaded region are the mean and standard error of 4 replicates with different random seeds. Overall, the training of vsOED is highly stable, with consistent performance across different random seeds, except for a dip in the training of vsOED-G-T. Table 23 presents the evaluation of optimal policies from 4 replicates optimized for horizon  $N = 10$ . Each element in the table represents the mean and standard error computed from  $3 \times 10^5$  samples. Table 24 further provides the mean and standard error aggregated from the means of these 4 replicates, further supporting the robustness of vsOED in the SIR problem.

**Policies.** Fig. 19 shows the trajectories and designs of 3 realizations of  $(\beta, \rho)$  with different ratios  $R = \beta/\rho$ . Smaller  $R$  corresponds to a more spreading design, which aligns with the results in [30].

More results about the SIR model problem can be found in Sec. 6.2 in the main paper.

## C.7 Convection-diffusion

This experiment is similar to the source location finding case in Appendix C.4, and was previously studied in [50] for the uni-model example. Here we consider  $M = 3$  candidate models with uniform

Table 22: Hyperparameters for the SIR problem.

	vsOED-G-T	vsOED-F-T
#training iteration $n_{\text{update}}$	10001	10001
#new episodes per iteration $n_{\text{episode}}$	1000	1000
batch size $n_{\text{batch}}$	10000	10000
parameter predictor initial lr	$5 \times 10^{-4}$	$10^{-3}$
parameter predictor lr decay	0.9999	0.9999
#param predictor update per iteration	5	5
$n_{\text{mixture}}$	8	N/A
$n_{\text{trans}}$	N/A	4
initial actor lr	$5 \times 10^{-4}$	$5 \times 10^{-4}$
actor lr decay	0.9999	0.9999
initial critic lr	$10^{-3}$	$10^{-3}$
critic lr decay	0.9999	0.9999
max buffer size	$10^6$	$10^6$
discount factor $\gamma$	1	1
initial design noise scale	5	5
design noise scale decay	0.9999	0.9999
target network lr	0.1	0.1

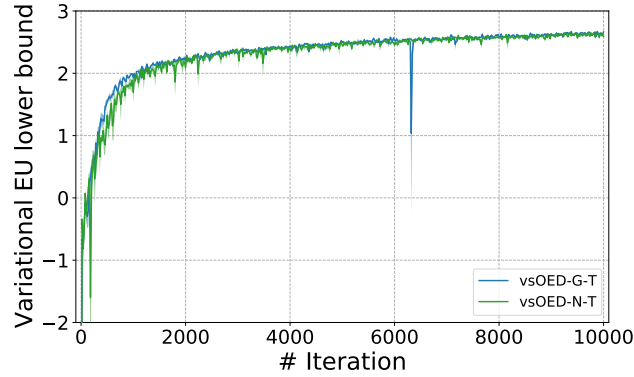


Figure 18: Training histories for the SIR problem, optimized for horizon  $N = 10$ . The solid line and the shaded region are the mean and standard error of 4 replicates with different random seeds.

Table 23: Variational expected utility lower bounds of optimal policies from 4 replicates for the SIR problem, optimized for horizon  $N = 10$ .

	Run 1	Run 2	Run 3	Run 4
vsOED-G-T	$4.091 \pm 0.002$	$4.093 \pm 0.002$	$4.090 \pm 0.001$	$4.092 \pm 0.001$
vsOED-F-T	$4.097 \pm 0.002$	$4.100 \pm 0.002$	$4.091 \pm 0.002$	$4.106 \pm 0.002$

Table 24: Aggregated variational expected utility lower bounds of optimal policies from 4 replicates for the SIR problem, optimized for horizon  $N = 10$ .

	Mean	SE
vsOED-G-T	4.092	0.001
vsOED-F-T	4.099	0.003

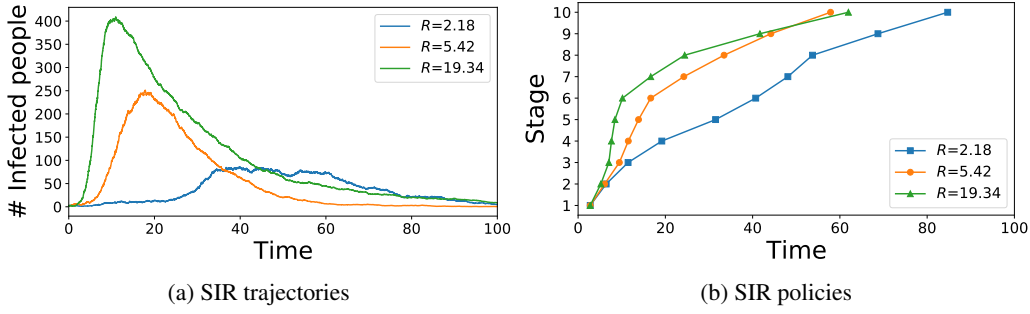


Figure 19: (a) SIR trajectories for 3 realizations of  $(\beta, \rho)$  with different ratios  $R = \beta/\rho$ . (b) Corresponding designs.

prior model probability (i.e.  $P(m) = 1/3$ ). For the  $m$ th model ( $m \in \{1, 2, 3\}$ ), there are  $m$  chemical contaminant sources randomly located in a 2D domain. Instead of an analytical function to describe the source signal, here the contaminant concentration at a given time  $t$  and a location  $\xi = [\xi_x, \xi_y] \in \mathbb{R}^2$  is determined by a convection-diffusion partial differential equation (PDE). Specifically, for the  $m$ th model:

$$\frac{\partial G(\xi, t; m, \theta_m, \eta_m)}{\partial t} = \nabla^2 G - u(\eta_m) \cdot \nabla G + S(\xi, t; m, \theta_m), \quad \xi \in [-1, 2]^2, \quad 0 \leq t \leq 0.2,$$

where  $u = [v \cos \beta, v \sin \beta] \in \mathbb{R}^2$  is the convection velocity that is described by nuisance parameters  $\eta_m$ , which encompasses the convection speed (magnitude)  $v \sim \mathcal{U}[0, 20]$  and the convection angle  $\beta \sim \mathcal{U}[0, 2\pi]$ . The source function is

$$S(\xi, t; m, \theta_m) = \sum_{i=1}^m \frac{s}{2\pi h^2} \exp\left(-\frac{\|\theta_{m,i} - \xi\|^2}{2h^2}\right),$$

where the PoIs  $\theta_m = \{\theta_{m,1}, \dots, \theta_{m,m}\}$  entails the source locations for  $m$ th model,  $s = 2$  is the known source strength, and  $h = 0.05$  is the known source width. The initial condition of the PDE is  $G(\xi, 0; m, \theta_m, \eta_m) = 0$  and homogeneous Neumann boundary conditions are applied to all sides of the domain. The PoI prior is

$$\theta_{m,i,x}, \theta_{m,i,y} \sim \mathcal{U}[0, 1],$$

and the observation model is

$$y \sim \mathcal{N}(G(d, t; m, \theta_m, \eta_m), \sigma^2),$$

with  $\sigma = 0.05$  being the observation noise standard deviation, and  $d = [d_x, d_y] \in [0, 1]^2$  the design variable is the sensor locations for taking measurements.

Similar to Appendix C.4, we are interested in the integrated flux at the right boundary and at a future time  $t = 0.2$ , with the formula

$$J(m, \theta_m, \eta_m) = \int_{\xi_y=0}^1 -\frac{\partial G((\xi_x = 1, \xi_y), t = 0.2; m, \theta_m, \eta_m)}{\partial \xi_x} d\xi_y,$$

and the overall goal-oriented QoI is  $z_m = \log(|J(m, \theta_m, \eta_m)| + 10^{-27})$ .

The OED problem involves designing a sequence of  $N$  sensor locations over time (i.e. relocation movements), where the  $k$ th experiment is performed at time  $t_k = 0.01(k + 1)$ . Moreover, we assume that the initial sensor location is at  $\xi_0 = [0.5, 0.5]$ , and we incorporate a sensor movement penalty to the immediate rewards to reflect the cost of moving. For stage  $k = 0$ , the penalty is  $-0.1 \|\xi_0 - \xi_0\|$ , and for stage  $k = 1, \dots, N - 1$ , the penalty is  $-0.1 \|\xi_k - \xi_{k-1}\|$ ; hence, a further movement would incur a higher cost.

**Surrogate model.** To solve the convection-diffusion PDE, we employ the second-order finite volume method on a uniform grid. The grid has a size of  $\Delta \xi_x = \Delta \xi_y = 0.01$ , ensuring a consistent spatial

discretization. For time integration, we utilize the second-order fractional step method with a time step of  $\Delta t = 5.0 \times 10^{-4}$ . The flux can be easily computed by applying the finite difference to the grids near the right boundary.

While using the numerical PDE solver as the forward model is possible, it can be computationally expensive and wasteful, since the numerical PDE solver solves for the concentration over the entire domain, while only a small subset of these values are used in the forward model. Therefore, to accelerate the computation, we pre-build NN surrogate forward models of  $G(\xi, t_k; m, \theta_m, \eta_m)$  for each  $m$ th model and at each  $t_k$  for  $k = 0, \dots, N - 1$ . We also build NN surrogate goal-oriented prediction models of  $J(m, \theta_m, \eta_m)$  for each  $m$ th model. The architecture of the surrogate forward and prediction models are summarized in Table 25 and 26. 20,000 simulations are generated with random  $\theta_m$  and  $\eta_m$  for each  $m$ th model. From these, 18,000 are used for training, and 2000 for testing. The testing mean squared errors (MSE) are summarized in Table 27. Figure 20 presents comparisons of true and surrogate model predicted concentration fields, indicating good agreement.

Table 25: Architecture of the surrogate forward model.

Layer	Description	Dimension	Activation
Input	$[\theta_m, \eta_m, \xi]$	$2m + 4$	-
H1	Dense	256	ReLU
H2	Dense	256	ReLU
H3	Dense	256	ReLU
H4	Dense	256	ReLU
Output	Dense	1	-

Table 26: Architecture of the surrogate prediction model.

Layer	Description	Dimension	Activation
Input	$[\theta_m, \eta_m]$	$2m + 2$	-
H1	Dense	256	ReLU
H2	Dense	256	ReLU
H3	Dense	256	ReLU
Output	Dense	1	-

Table 27: Testing MSE of surrogate models.

Model	surrogate forward model	surrogate prediction model
$m = 1$	$3.094 \times 10^{-5}$	$4.141 \times 10^{-5}$
$m = 2$	$3.284 \times 10^{-4}$	$4.986 \times 10^{-4}$
$m = 3$	$1.650 \times 10^{-3}$	$2.080 \times 10^{-3}$

**Hyperparameters.** The hyperparameters are listed in Table 28. We only use vsOED with the TIG formulation. For the linear mapping in the output layer of the GMM net, we transform the output of the GMM mean net of the PoI posterior predictor to a range of  $[-1, 2]$ , and the output of the GMM standard deviation net of the PoI posterior predictor to a range of  $[10^{-5}, 1]$  for all PoIs. For the goal-oriented QoI posterior predictor, we transform the output of the GMM mean net to a range of  $[-15, 3]$ , and the output of the GMM standard deviation net to a range of  $[10^{-5}, 4]$ . The truncated normal distribution is used on all PoIs with support  $[0, 1]$ .

Similar to the multi-model source location finding problem, 5 scenarios will be considered: model discrimination OED ( $\alpha_M = 1, \alpha_\Theta = \alpha_Z = 0$ ), inference OED ( $\alpha_\Theta = 1, \alpha_M = \alpha_Z = 0$ ), goal-oriented OED ( $\alpha_Z = 1, \alpha_M = \alpha_\Theta = 0$ ), discrimination-inference OED ( $\alpha_M = \alpha_\Theta = 1, \alpha_Z = 0$ ) and discrimination-goal-oriented OED ( $\alpha_M = \alpha_Z = 1, \alpha_\Theta = 0$ ).

**Training stability.** The investigation of training stability is illustrated here only on the inference OED scenario. Figure 11 shows the training histories of the inference OED, where the solid line and the shaded region are the mean and standard error of 4 replicates with different random seeds.

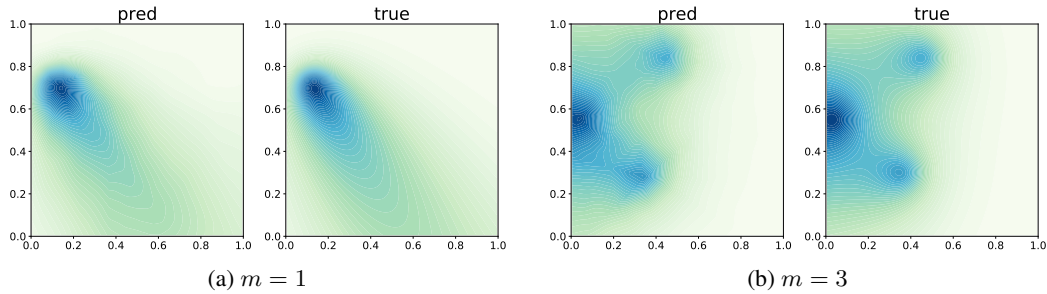


Figure 20: Example comparisons between true and surrogate model predicted concentration fields.

Table 28: Hyperparameters for the convection-diffusion problem.

	vsOED-G-T
#training iteration $n_{\text{update}}$	10001
#new episodes per iteration $n_{\text{episode}}$	1000
batch size $n_{\text{batch}}$	10000
model predictor initial lr	$10^{-3}$
model predictor lr decay	0.9999
#model predictor update per iteration	5
parameter predictor initial lr	$10^{-3}$
parameter predictor lr decay	0.9999
#param predictor update per iteration	5
$n_{\text{mixture}}$	8
initial actor lr	$5 \times 10^{-4}$
actor lr decay	0.9999
initial critic lr	$10^{-3}$
critic lr decay	0.9999
max buffer size	$10^6$
discount factor $\gamma$	1
initial design noise scale	0.05
design noise scale decay	0.9999
target network lr	0.1

Note that the prior term is omitted due to the presence of nuisance parameters. Table 29 presents the variational lower bounds evaluated for optimal policies from 4 replicates of inference OED, optimized for horizon  $N = 10$ . Each element in the table represents the mean and standard error computed from  $10^6$  samples. Table 30 further provides the mean and standard error aggregated from the means of these 4 replicates. From these results, vsOED demonstrates excellent robustness under different random seeds.

Table 29: Variational lower bounds evaluated for optimal policies from 4 replicates of inference OED for the convection-diffusion problem, optimized for horizon  $N = 10$ .

	Run 1	Run 2	Run 3	Run 4
vsOED-G-T	$2.998 \pm 0.002$	$3.057 \pm 0.002$	$2.857 \pm 0.002$	$3.039 \pm 0.002$

**Expected utilities.** Figure 22 plots the expected utilities of various OED scenarios, averaged over 2 replicates.

**Policies.** Figure 23 plots example designs of various OED scenarios optimized for horizon  $N = 10$ . The overall behavior is similar to the multi-model source location finding problem, except they now appear more exploratory.

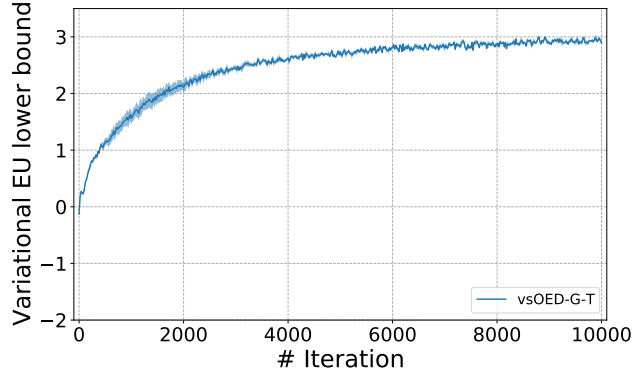
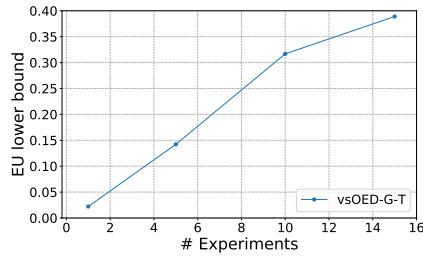


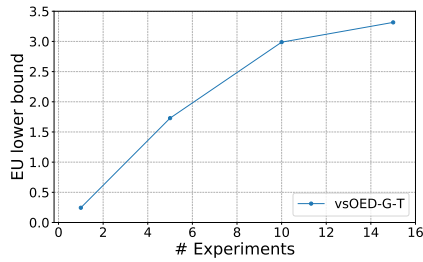
Figure 21: Training histories of inference OED for the convection-diffusion problem, optimized for horizon  $N = 10$ . The solid line and the shaded region are the mean and standard error of 4 replicates with different random seeds.

Table 30: Aggregated variational lower bounds evaluated for optimal policies from 4 replicates of inference OED for the convection-diffusion problem, optimized for horizon  $N = 10$ .

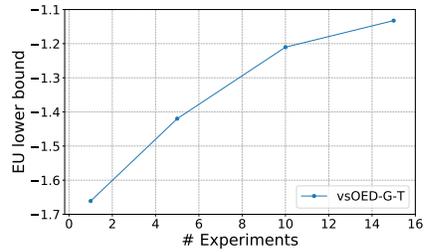
	Mean	SE
vsOED-G-T	2.988	0.039



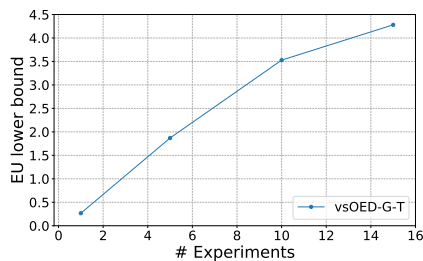
(a) Model discrimination OED



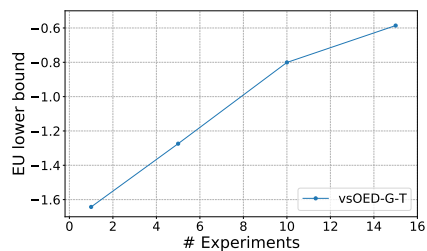
(b) Inference OED



(c) Goal-oriented OED

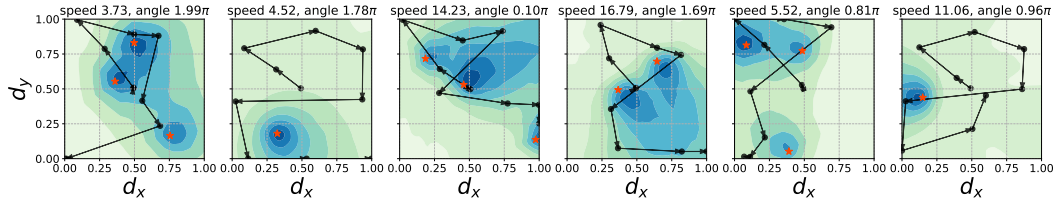


(d) Discrimination-inference OED

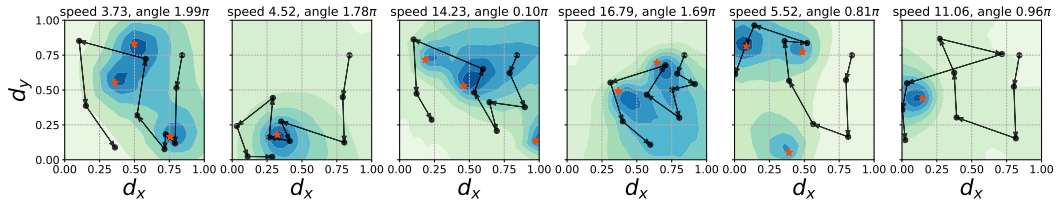


(e) Discrimination-goal-oriented OED

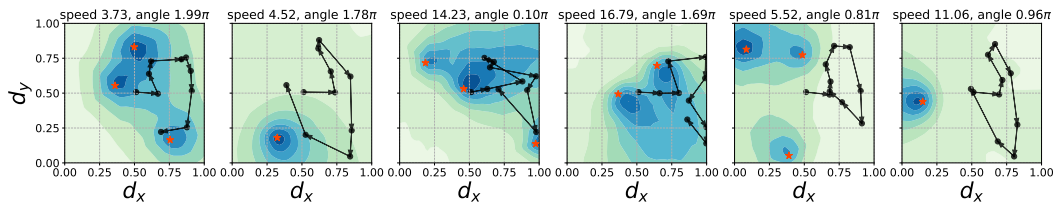
Figure 22: Expected utilities of various OED scenarios, averaged over 2 replicates. Variational lower bounds are evaluated using  $10^6$  samples.



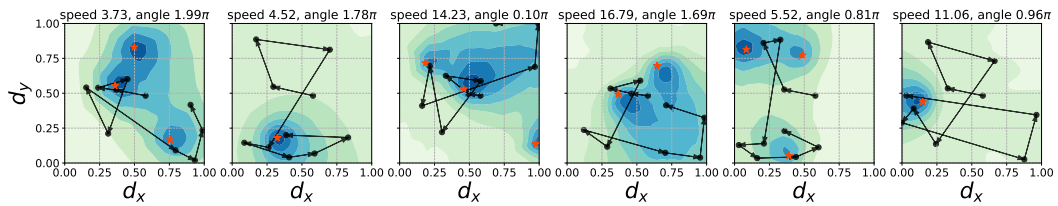
(a) Model discrimination OED



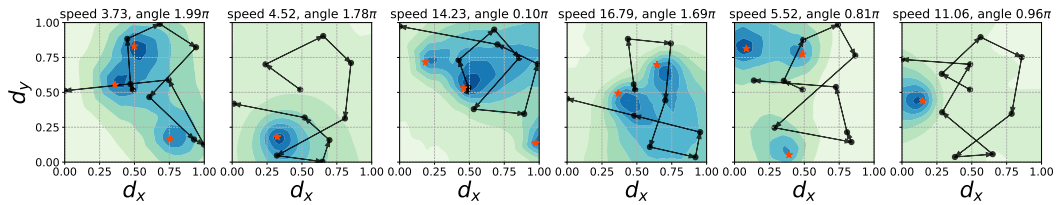
(b) Inference OED



(c) Goal-oriented OED



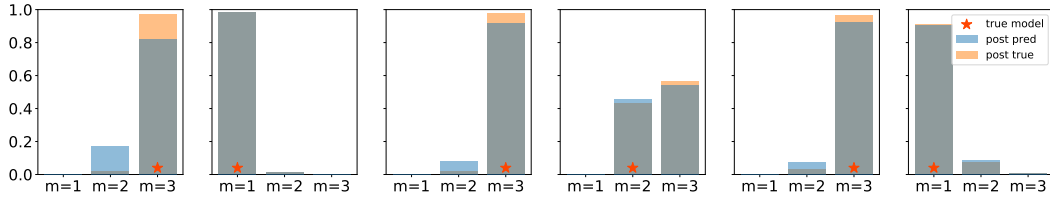
(d) Discrimination-inference OED



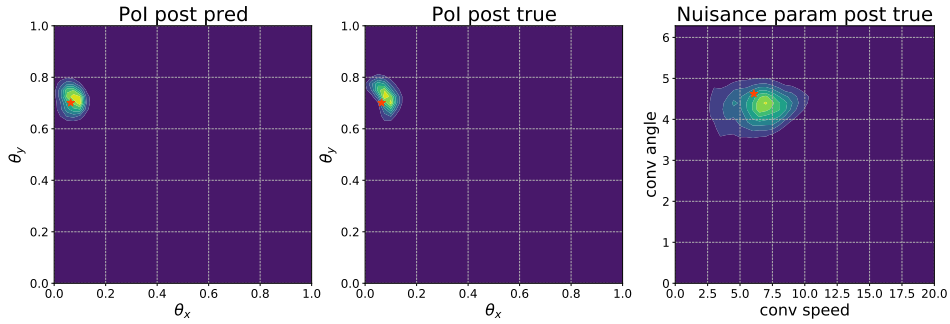
(e) Discrimination-goal-oriented OED

Figure 23: Example designs of various OED scenarios of the convection-diffusion problem, optimized for horizon  $N = 10$ .

**Posteriors.** Figure 24 illustrates the model and PoI posteriors of the model discrimination OED and inference OED optimized for horizon  $N = 10$ . The model posterior predictor and GMM both effectively approximate their true posteriors.



(a) Model posteriors from the model discrimination OED scenario



(b) Parameter posteriors at  $m = 1$  from the inference OED scenario

Figure 24: Example model and parameter posteriors from the model discrimination OED and inference OED for the convection-diffusion problem optimized for horizon  $N = 10$ .

For more results about the convection-diffusion problem see Sec. 6.3 in the main paper.